



## RESEARCH ARTICLE

# Linear multi-scale modeling of diffusion MRI data: A framework for characterization of oriented structures across length scales

Barbara D. Wichtmann<sup>1,2</sup>  | Qiuyun Fan<sup>1,3</sup>  | Laleh Eskandarian<sup>1</sup> |  
 Thomas Witzel<sup>4</sup> | Ulrike I. Attenberger<sup>2</sup> | Claus C. Pieper<sup>2</sup> | Lothar Schad<sup>5</sup> |  
 Bruce R. Rosen<sup>1</sup> | Lawrence L. Wald<sup>1,6</sup> | Susie Y. Huang<sup>1,6</sup> | Aapo Nummenmaa<sup>1</sup>

<sup>1</sup>A. A. Martinos Center for Biomedical Imaging, Department of Radiology, Massachusetts General Hospital, Charlestown, Massachusetts, USA

<sup>2</sup>Department of Diagnostic and Interventional Radiology, University Hospital Bonn, Bonn, Germany

<sup>3</sup>Department of Biomedical Engineering, College of Precision Instruments and Optoelectronics Engineering, Tianjin University, Tianjin, China

<sup>4</sup>Q Bio Inc., San Carlos, California, USA

<sup>5</sup>Computer Assisted Clinical Medicine, Mannheim Institute for Intelligent Systems in Medicine, Medical Faculty Mannheim, Heidelberg University, Mannheim, Germany

<sup>6</sup>Harvard-MIT Division of Health Sciences and Technology, Massachusetts Institute of Technology, Cambridge, Massachusetts, USA

## Correspondence

Barbara D. Wichtmann, Department of Diagnostic and Interventional Radiology, University Hospital Bonn, Venusberg-Campus 1, D-53127 Bonn, Germany.  
 Email: [barbara.wichtmann@ukbonn.de](mailto:barbara.wichtmann@ukbonn.de)

## Funding information

National Institutes of Health, Grant/Award Numbers: K23-NS096056, P41-EB017183, P41-EB030006, R00EB015445, R01-NS118187, R01MH111829, U01-EB026996; National Natural Science Foundation of China, Grant/Award Number: NSFC 82071994

## Abstract

Diffusion-weighted magnetic resonance imaging (DW-MRI) has evolved to provide increasingly sophisticated investigations of the human brain's structural connectome in vivo. Restriction spectrum imaging (RSI) is a method that reconstructs the orientation distribution of diffusion within tissues over a range of length scales. In its original formulation, RSI represented the signal as consisting of a spectrum of Gaussian diffusion response functions. Recent technological advances have enabled the use of ultra-high  $b$ -values on human MRI scanners, providing higher sensitivity to intracellular water diffusion in the living human brain. To capture the complex diffusion time dependence of the signal within restricted water compartments, we expand upon the RSI approach to represent restricted water compartments with non-Gaussian response functions, in an extended analysis framework called linear multi-scale modeling (LMM). The LMM approach is designed to resolve length scale and orientation-specific information with greater specificity to tissue microstructure in the restricted and hindered compartments, while retaining the advantages of the RSI approach in its implementation as a linear inverse problem. Using multi-shell, multi-diffusion time DW-MRI data acquired with a state-of-the-art 3 T MRI scanner equipped with 300 mT/m gradients, we demonstrate the ability of the LMM approach to distinguish different anatomical structures in the human brain and the potential to advance mapping of the human connectome through joint estimation of the fiber orientation distributions and compartment size characteristics.

## KEYWORDS

diffusion, human brain, In vivo, LMM, microstructure imaging, MRI, Time-dependent DWI

Barbara D. Wichtmann and Qiuyun Fan have contributed equally to this study. Susie Y. Huang and Aapo Nummenmaa were considered as joint senior authorship.

This is an open access article under the terms of the [Creative Commons Attribution-NonCommercial-NoDerivs](https://creativecommons.org/licenses/by-nc-nd/4.0/) License, which permits use and distribution in any medium, provided the original work is properly cited, the use is non-commercial and no modifications or adaptations are made.

© 2022 The Authors. *Human Brain Mapping* published by Wiley Periodicals LLC.

## 1 | INTRODUCTION

Over the last three decades, diffusion-weighted magnetic resonance imaging (DW-MRI) has evolved to provide increasingly sophisticated investigations of tissue microstructure in the living human brain. The methodological basis for using water diffusion to estimate the properties of porous media is well established (Callaghan, 1993; Callaghan & Stepisnik, 1995), and the application of DW-MRI to the biophysical domain has been demonstrated in various tissue preparations and animal models in small-bore scanners (Assaf et al., 2008; Barazany et al., 2009; Basser et al., 1994; Ong & Wehrli, 2010; Stanisz et al., 1997). However, using DW-MRI for in-vivo mapping of human brain tissue microstructure has required technical development efforts in several key areas. The main barrier to pushing the diffusion resolution for human imaging has been the traditionally limited gradient performance of human MRI scanners. This hardware limitation has been addressed through the introduction of high-performance gradient systems for human imaging (Foo et al., 2020; Vachha & Huang, 2021; van Essen et al., 2012), including dedicated engineering of the Connectome MRI scanner (Fan et al., 2014; Fan et al., 2016; Huang et al., 2015; Jones et al., 2018; McNab et al., 2013; Setsompop et al., 2013), which was the first of its kind to incorporate a 300 mT/m whole-body gradient coil into a wide-bore 3 T scanner platform. When combined with parallel imaging acquisition and reconstruction techniques such as Simultaneous Multi-Slice (SMS) (Feinberg et al., 2010; Feinberg & Setsompop, 2013; Setsompop, Cohen-Adad, et al., 2012a; Setsompop, Gagoski, et al., 2012b) and Fast Low-angle Excitation Echo-planar Technique (FLEET) (Polimeni et al., 2016), as well as appropriate post-processing methods (Andersson et al., 2016; Andersson & Sotiropoulos, 2015), such hardware advances have enabled the acquisition of extensive diffusion imaging datasets showing that reproducible estimation of an apparent axon diameter index is indeed feasible and requires high gradient amplitudes to sensitize the DW-MRI signal to intra-axonal water diffusion (Fan et al., 2021; Huang et al., 2015; Huang et al., 2020; Veraart et al., 2020).

The microstructural features of interest such as the axonal compartment sizes ( $\sim\mu\text{m}$ ) are orders of magnitude smaller than the size of the imaging voxel ( $\sim\text{mm}$ ). Therefore, the process of mapping these quantities relies on inferring this information indirectly, usually by means of compartmental modeling of the acquired signals (Afzali et al., 2021; Alexander et al., 2019; Duval et al., 2016; Henriques et al., 2021; Jelescu et al., 2020; Kiselev, 2021; Nilsson et al., 2018; Novikov, 2021; Novikov et al., 2019; Novikov, Kiselev, & Jespersen, 2018a; Novikov, Veraart, et al., 2018b; Panagiotaki et al., 2012; Szczepankiewicz et al., 2021; Xu, 2021). In a widely used model (Assaf & Basser, 2005), the axons are assumed to be impermeable cylindrical elements characterized by non-Gaussian restricted diffusion that are surrounded by a Gaussian extracellular diffusion compartment. Estimating the parameters of the non-linear model can be achieved by Markov-Chain-Monte-Carlo (MCMC)-based methods originally presented in the context of optimization of experimental design for microstructural DW-MRI (Alexander, 2008). While

computationally intensive, the MCMC approach can be used to avoid local minima as well as to quantify the parameter uncertainty in the Bayesian sense, resulting in robust estimates for this inherently low-SNR problem. However, the basic MCMC approach works well when the number of the parameters is relatively small, requiring separation of the estimation task into two sub-problems (Alexander et al., 2010; Huang et al., 2020): (i) estimation of the fiber orientation distribution function, and (ii) estimating the microstructural parameters themselves assuming the fiber orientations are known. Alternatively, the orientation dependence of the signals can be removed by spherical averaging (Kaden, Kelm, et al., 2016a; Kaden, Kruggel, & Alexander, 2016b) that has been recently demonstrated to result in axon diameter index estimates independent of fiber orientation (with real-valued data to remove the Rician noise build-up) (Fan et al., 2020; Veraart et al., 2020). However, the MCMC technique requires long computational times, and the spherical averaging results in partial loss of the information present in the data, retaining only the first order spherical harmonics coefficients (Fan et al., 2020). The fitting of multi-compartment microstructural models to extract biophysical parameters is a complex problem that has been achieved using a variety of non-linear optimization methods and initialization strategies (Harms et al., 2017). Here, we investigate an alternative solution strategy to explore the full multi-shell diffusion data by means of a linear inverse problem formulation with joint estimation of length scale and orientation information.

Restriction spectrum imaging (RSI) is an extension of the well-known linear spherical deconvolution model (Tournier et al., 2004). In its original formulation, RSI reconstructed the diffusion tissue orientation distribution over a range of length scales by assuming a spectrum of Gaussian diffusion response functions (White, Leergaard, et al., 2013a). The RSI model provides estimates of both the orientational and length scale information while imposing few assumptions about the underlying tissue microstructure and offering a linear implementation that is computationally efficient and straightforward. However, with the use of high b-value diffusion acquisitions the non-Gaussian properties of water diffusion become more pronounced, which are important for gaining sensitivity to restricted (i.e., intra-axonal/intracellular) water diffusion (Huang et al., 2015; Veraart et al., 2019).

Using a state-of-the-art 3 T MRI scanner equipped with 300 mT/m gradients, in this work we expand upon the RSI approach to fully capture the complex time dependence of the diffusion signal arising from restricted compartments that is represented with non-Gaussian response functions. In this extended analysis framework, called linear multi-scale modeling (LMM), we incorporate two types of response functions: (1) a non-Gaussian diffusion response function to account for restricted diffusion in the intracellular/intra-axonal space; and (2) Gaussian diffusion response functions to model hindered diffusion in the extracellular compartment and free diffusion in cerebrospinal fluid (CSF). The goal of the LMM approach is to solve for length scale and orientation-specific information with greater specificity to tissue microstructure in the restricted and hindered compartments while preserving the advantages of the RSI approach in formulating

the analysis as a straightforward linear inverse problem. Using multi-shell, multi-diffusion time DW-MRI data, we demonstrate the ability of the LMM approach to distinguish different anatomical structures in the human brain in a cohort of healthy volunteers and to probe neural architecture in vivo. By explicitly incorporating restricted diffusion into the model, the extended LMM framework enables an improved overall separation between restricted and hindered water compartments. Furthermore, by employing the Connectome MRI scanner we are able to probe the regime in which the diffusion signal is sensitive to the finite size of the restricted compartment, thereby enabling the LMM approach to also capture information on the apparent axon diameter. We show that our measurements are sensitive to specific microstructural tissue features by comparing our results with known histological differences of distinct brain regions. The estimation of restricted and hindered volume fractions and compartment sizes could allow for the development of distinct microstructural signatures of healthy and diseased tissue. Finally, the information obtained on the orientation distribution at different length scales could provide further insight into the structural connectivity of the brain.

## 2 | MATERIALS AND METHODS

### 2.1 | Signal models

#### 2.1.1 | LMM

The mathematical model of the LMM framework explicitly characterizes diffusion in restricted, hindered and free water compartments of different size and orientation. The total DW-signal  $S$  is expressed as a

convolution over the unit sphere of each water compartment's response function  $R$  with its corresponding orientation distribution  $f$  (Figure 1). A detailed description of the methodology and LMM algorithm can be found in the Appendix S1.

In short, for the different sized restricted water compartments non-Gaussian diffusion response functions  $R_R$  are employed that describe the DW-signal arising from water molecules within impermeable cylinders of increasing diameter  $a$ . Axially symmetric Gaussian diffusion response functions  $R_H$  with a fixed longitudinal diffusivity  $D_L$  and increasing transverse diffusivity  $D_T$  are used to model the DW-signal arising from the different sized extracellular, hindered water compartments. To model the partial volume fraction of free water diffusion, an isotropic Gaussian diffusion response function  $R_F$  was included with free water diffusivity  $D_F$ . Thus, the oriented component of the DW signal equals the sum of each water compartment's response function, weighted by their respective volume fraction and oriented along their respective orientation:

$$S = R_R(a_1)f_{R_1} + R_R(a_2)f_{R_2} + \dots + R_R(a_5)f_{R_5} + R_H(D_{T_1})f_{H_1} + R_H(D_{T_2})f_{H_2} + \dots + R_H(D_{T_5})f_{H_5} + R_F(D_F)f_F.$$

#### 2.1.2 | Spectrum of Gaussian diffusion functions

RSI (White, Leergaard, et al., 2013a) is a method that reconstructs the diffusion tissue orientation distribution over a spectrum of length scales by assuming a spectrum of Gaussian diffusion response functions. To investigate the impact of mathematically accounting for restricted diffusion by non-Gaussian diffusion response functions, the LMM approach was compared with an analysis performed for a

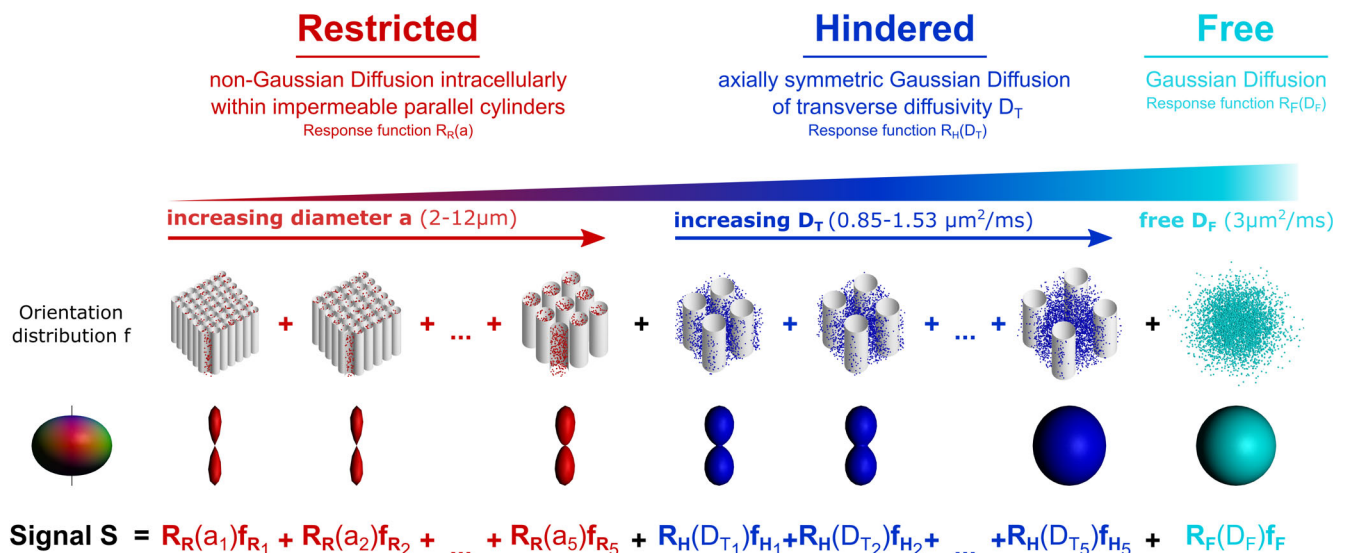


**FIGURE 1** The Linear Multi-Scale Model. The linear multi-scale forward model of different sized restricted and hindered diffusion compartments is obtained by concatenating two spectra of response functions: (1) a non-Gaussian diffusion response function for water restricted inside cylindrical structures and (2) a Gaussian diffusion response function for hindered water and free water diffusion. The diffusion-weighted signal equals the sum of each water compartment's response function  $R$  convoluted with its corresponding orientation distribution  $f$ . Each compartment's orientation distribution is parameterized with spherical harmonics

spectrum of Gaussian functions akin to the RSI method. This approach reduces to a spectrum of axially symmetric Gaussian response functions in the form of:

$$S = R(D_{T_1})f_1 + R(D_{T_2})f_2 + \dots + R(D_{T_{10}})f_{10} + R_F(D_F)f_F.$$

## 2.2 | Simulation data

Synthetic DW-MRI data was generated by simulating the random walk of spins/molecules within different restricting 3D-environments using the Monte Carlo diffusion simulator of Camino (Cook et al., 2006; Hall & Alexander, 2009). Our substrates consisted of either vertically or horizontally, hexagonally packed, parallel, non-overlapping, impermeable cylinders of a single diameter and fixed intracellular, that is, within the cylinders, volume fraction. Cylinder diameters were simulated ranging from 1  $\mu\text{m}$  up to 14  $\mu\text{m}$  and intracellular volume fractions ranging from 0.3 to 0.7 for an infinite signal-to-noise ratio (SNR). To synthesize substrates with fibers of different diameters crossing at 90°, the signals from the vertically and horizontally simulated parallel cylinders with an intracellular volume fraction of 0.7 were added up proportionally to 100%.

Subsequently, Rician noise of an SNR of 20 was added to the noise free data. To ensure reproducibility of our synthetic signal we used 100,000 walkers and 5001 time steps in each simulation. The intrinsic diffusivity  $D$  was set to  $D_L = 1.7 \cdot 10^{-9} \text{m}^2 \text{s}^{-1}$ , corresponding to the longitudinal diffusivity along the principal diffusion direction in the human corpus callosum in vivo (Fan et al., 2020). A PGSE sequence with the same parameters as the in vivo imaging protocol (see below) was used to generate the synthetic data.

## 2.3 | Data acquisition

With approval from the institutional review board, 16 healthy volunteers (mean age  $39 \pm 18$  years) were scanned on a dedicated high-gradient 3 T MRI scanner (MAGNETOM CONNECTOM, Siemens Healthineers, Erlangen, Germany) with a maximum gradient strength of 300 mT/m and maximum slew rate of 200 T/m/s. A custom-made 64-channel phased array head coil was used for signal reception (Keil et al., 2013).

The DW-MRI acquisition with whole brain coverage was performed using a monopolar Stejskal–Tanner pulsed gradient spin echo (PGSE), echo planar imaging (EPI) sequence with the following parameters: echo time (TE)/repetition time (TR) = 77/[3600–4000] ms, 2 mm isotropic resolution, two diffusion times  $\Delta = 19$  and 49 ms, diffusion gradient pulse duration  $\delta = 8$  ms, eight diffusion encoding gradient strengths evenly spaced between 30 and 290 mT/m, 32 diffusion encoding directions uniformly distributed on a sphere for  $b < 2400 \text{ s/mm}^2$ , 64 diffusion encoding directions for  $b \geq 2400 \text{ s/mm}^2$ , parallel imaging acceleration factor  $R = 2$  (GRAPPA), partial Fourier of 7/8, simultaneous multislice acceleration factor of 2 (Setsompop, Gagoski, et al., 2012b), and anterior-to-posterior phase encoding.

The applied  $b$ -values at  $\Delta = 19$  ms were  $b = 50, 350, 800, 1500, 2400, 3450, 4750, 6000 \text{ s/mm}^2$ , and at  $\Delta = 49$  ms  $b = 200, 950, 2300, 4250, 6750, 9850, 13500, 17800 \text{ s/mm}^2$ . Interspersed  $b = 0$  images were acquired every 16 DW-images. In addition, a set of five  $b = 0$  images with reversal of the phase encoding direction were acquired separately to correct for geometric distortions due to susceptibility effects and eddy currents. For registration and segmentation, a high-resolution three-dimensional T1-weighted (T1w) multi-echo magnetization-prepared rapid gradient echo (MEMPRAGE) sequence was also acquired in each study using  $1 \times 1 \times 1 \text{ mm}^3$  voxels, TR/TE = 2530/[1.15, 3.03, 4.89, 6.75] ms, inversion time = 1100 ms, and  $R = 2$ . The DW-MRI sequence was adapted to export phase images in addition to the magnitude images. The total MRI acquisition time was approximately 55 min.

## 2.4 | Data preprocessing and segmentation

The magnitude and phase data acquired in the DW-MRI experiments were used to calculate the real-valued data by removing the nuisance background phase, with Gaussian-distributed noises remaining in the resulting imaging data (Eichner et al., 2015; Fan et al., 2020). The real-valued diffusion data was then corrected for gradient nonlinearity distortion using in-house developed MATLAB tools (Fan et al., 2016; Glasser et al., 2013; Jovicich et al., 2006), followed by correction for susceptibility- and eddy current-induced distortions using the TOPUP (Andersson et al., 2003) and EDDY (Andersson et al., 2016; Andersson & Sotiropoulos, 2016) functions in the FMRIB Software Library toolboxes (Smith et al., 2004) (FSL, version 5.0.9, <https://fsl.fmrib.ox.ac.uk>).

The T1w images were also corrected for gradient nonlinearity distortions and then processed with the automated cortical parcellation and subcortical segmentation tools in FreeSurfer (Fischl et al., 2002) (stable version v6.0.0, <http://surfer.nmr.mgh.harvard.edu>) to generate masks of cerebral gray matter, white matter, and subcortical nuclei for region-of-interest (ROI) analyses.

## 2.5 | Signal approximation with spherical harmonics

For noise reduction and improving the numerical conditioning of the inverse problem, expansion of the real spherical harmonics up to order  $\ell = 6/\ell = 8$  with Laplace–Beltrami regularization was used to interpolate and smoothen the diffusion signal on each  $q$ -shell with  $\leq 64$  gradient directions/with more than 64 directions (Descoteaux et al., 2007). The regularization parameter  $\lambda$  was set to 0.006.

## 2.6 | Model fitting and data analysis

Voxel-wise fitting of the DW-MRI data was performed in the native space of each subject. To obtain the orientation distribution functions

and corresponding signal fractions, hereafter also referred to as volume fractions, of the different sized restricted and hindered water compartments, the signal arising from each compartment was deconvolved with the corresponding response function. For a more compact and efficient linear implementation we parameterized the orientation distribution functions of the Gaussian diffusion and non-Gaussian diffusion compartments with spherical harmonics up to order  $\ell = 4$  and  $\ell = 6$ , respectively (Descoteaux et al., 2007). The parameter  $D_L$  was set to  $1.7 \mu\text{m}^2/\text{ms}$  (Zhang et al., 2012) and  $D_F$  to the diffusion coefficient of free water at  $37^\circ\text{C}$ , that is,  $3 \mu\text{m}^2/\text{ms}$  similarly to earlier studies (Huang et al., 2015). For the LMM model we let the diameter  $a$  take on  $n_a = 5$  equally spaced values between 2 and  $12 \mu\text{m}$  and  $D_T$  was similarly discretized to  $n_{D_T} = 5$  hindered diffusion length scale values, equally spaced between 0.5 and  $0.9 D_L$  (see Appendix S1: further details on parameter selection). For the analysis performed for a spectrum of Gaussian functions,  $D_T$  was discretized to  $n = 10$  diffusion length scale values, linearly spaced between 0 and  $0.9 D_L$ . The multi-scale deconvolution inverse problem was solved by standard least-squares estimation with Tikhonov regularization.

## 2.7 | Group-averaged axon diameter maps

LMM analysis of the simulation data yielded distributions of volume fraction estimates for each simulated axon diameter. As already noted in (White, Leergaard, et al., 2013a), the linear inverse reconstruction results in “crosstalk” between length scales as the model does not make explicit assumptions about the number of fiber populations with different compartment diameter in each voxel. Therefore, in order to compare the LMM-based estimates with models where such assumption is made, we need to “convert” the volume fraction distributions to “single-axon” diameter estimates. To this end, the slope of the volume fraction estimates over the restricted diffusion length scales was considered to have a one-to-one correspondence to the simulated axon diameter, providing a “calibration curve”, that is, monotonic function, that allowed the corresponding average axon diameter per voxel to be determined for the *in vivo* data (see Figures S1).

Group-averaged maps were obtained as in Fan et al. (2020). Briefly, the registration process was comprised of two components—*intra-subject* registration between EPI images and T1w images, and *inter-subject* registration between each subject's native T1w image and the template T1w image. The *intra-subject* registration was performed using the boundary-based registration method (Greve & Fischl, 2009) with 6 degrees of freedom using the averaged interleaved  $b = 0$  image. The *inter-subject* registration was performed by morphing the T1w image of each subject to the cvs35 template in the FreeSurfer package using the Combined Volumetric and Surface (CVS) registration tool (Postelnicu et al., 2009; Zollei et al., 2010). The non-linear morph and the linear transformation were then simultaneously applied to the maps of apparent axon diameter in each subject's native space to obtain aligned maps in the cvs35 template space, which were then averaged over 15 subjects to derive a group averaged map. Group-averaged maps of the LMM analysis were compared

with group-averaged maps obtained using the spherical mean technique (SMT) as in Fan et al. (2020).

## 3 | RESULTS

### 3.1 | Simulation study

The LMM analysis of our simulation data yielded a fiber orientation distribution spectrum that tended to be consistent with the simulated cylinder diameters and volume fractions (Figures 2-4). For the simulated smaller axon diameters, that is,  $\leq 5 \mu\text{m}$ , the estimated volume fraction distributions looked relatively similar (Figure 2). Sensitivity of the LMM model to the compartment sizes increased with larger axon diameters. For a simulated voxel of densely packed impermeable cylinders with an intracellular volume fraction of 70% and an SNR of 20, the intracellular volume fraction was estimated to be 85% for a simulated axon diameter of  $2 \mu\text{m}$ , 83% for a simulated axon diameter of  $6 \mu\text{m}$ , 72% for a simulated axon diameter of  $10 \mu\text{m}$ , and 60% for a simulated axon diameter of  $14 \mu\text{m}$  (Figure 2). For simulated parallel, impermeable axons with a diameter of  $2 \mu\text{m}$ , an intracellular volume fraction of 30% and an SNR of 20, the restricted diffusion fraction was overestimated by 27%, to 57% (Figure 3). The larger the simulated cylinder diameters and the higher the packing density, the more accurate the LMM estimates of restricted diffusion became, exemplarily for simulated axons with a diameter of  $10 \mu\text{m}$  and an intracellular volume fraction of 70% the restricted diffusion fraction was estimated to be 72% (Figure 3). In comparison with the analysis performed for a spectrum of Gaussian functions (following the framework of the original RSI approach), the separation between the restricted length scales was enhanced by incorporating the non-Gaussian diffusion model. The LMM approach allowed for a direct, explicit read of the simulated axon diameter. For both analysis methods, there was some “crosstalk” between length scales such that the signal appeared to originate not only from the corresponding simulated length scale, but also from adjacent length scales. This observation became particularly evident in the simulation of crossing fibers with distinct cylinder diameters (Figure 4). While LMM was able to distinctly separate the orientation distribution of the different sized cylinders, we observed a substantial overlap of the signal fraction estimates originating from the different length scales (Figure 4).

### 3.2 | In vivo experiments

Figure 5 compares volume fraction maps of the LMM versus the analysis performed for a spectrum of Gaussian functions (akin the original RSI approach) for an exemplary axial slice at the level of the basal ganglia and lateral ventricles. We found a high degree of restriction particularly within the highly organized, densely packed WM. While LMM captured this trend across the 5 restricted length scales, almost all of the restricted diffusion signal in the approach using a spectrum of Gaussian functions appeared to be subsumed within the first(s)



## Linear Multi-scale Modeling

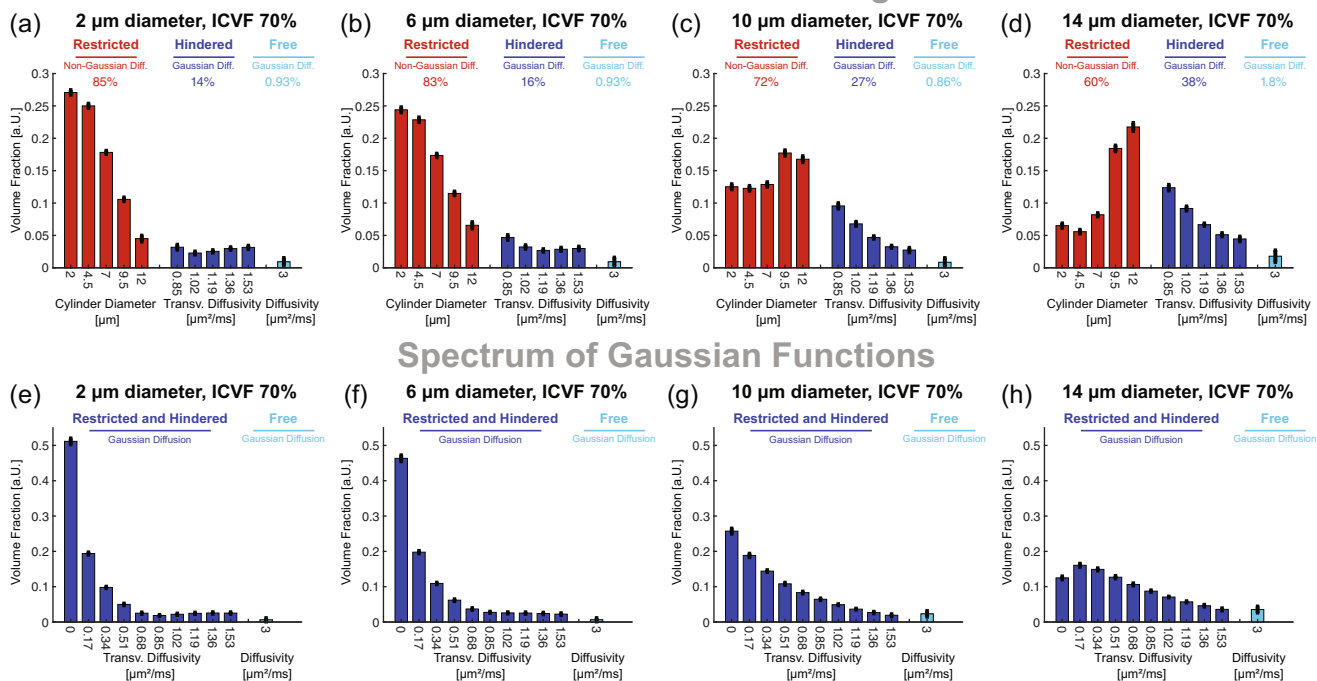


**FIGURE 2** Simulation results: LMM vs. an analysis performed for a spectrum of Gaussian functions. Shown are exemplary volume fraction estimates of the LMM analysis versus an analysis performed for a spectrum of Gaussian functions for a simulated voxel of tightly packed 2  $\mu\text{m}$  ((a), (e)), 6  $\mu\text{m}$  ((b), (f)), 10  $\mu\text{m}$  ((c), (g)) and 14  $\mu\text{m}$  ((d), (h)) impermeable cylinders with an intracellular volume fraction (ICVF) of 70% and an SNR of 20. Plotted are the mean and standard deviation of 500 different noise realizations. For the LMM analysis, the estimated volume fractions for the restricted, hindered, and free water diffusion compartments are provided in percentages ((a)-(d)). Incorporating the restricted diffusion model allows the LMM analysis framework to better distinguish the different sized restricted length scales. LMM is sensitive to simulated trends of cylinder diameters and volume fractions, though does not recover the ground truth entirely. Particularly, model sensitivity is limited for low diameter axons. For both analysis techniques, adjacent length scales blend into each other, suggesting that the signal arises not only from the corresponding simulated length scale but also from neighboring length scales

length scales. Within the cortical GM, the LMM volume fraction maps exhibited a high proportion of hindered water diffusion. Comparably, the volume fraction of larger length scales increased in the cortex for the approach using a spectrum of Gaussian functions. The free water signal nearly exclusively originated from the cerebrospinal fluid space. Taking the signal from all restricted, hindered, and free water compartments into their respective maps, LMM further highlighted the differences in diffusion behavior between WM and GM structures (Figure 6).

Voxel-wise estimated volume fraction distributions of the different sized water compartments were distinguishable between different anatomical structures within the brain. Figure 7 illustrates representative volume fraction estimates obtained by the LMM analysis for voxels within different WM and GM structures, concordant with the preceding volume fraction maps. The WM voxel displayed a high signal stemming primarily from the restricted diffusion water compartments, whereas the cortical GM voxel demonstrated a high signal arising from the hindered diffusion water length scales. The voxel within the thalamus contained a relatively high signal originating from both the restricted and hindered diffusion water compartments compared with WM and cortical GM. Figure 8 summarizes the voxel-wise volume fraction analysis for different regions of cortical and deep gray

matter by plotting the mean and standard deviation for the volume fraction estimates of each length scale within the respective regions. Consistent with the representative voxels, we observed a low fraction of restricted and high fraction of hindered diffusion within the cortex. We noted a slight increase of restricted diffusion for the first length scales in the caudate and putamen with an almost unchanged high proportion of hindered diffusion in comparison to the cortical GM. The thalamus and pallidum exhibited a mixture of restricted and hindered diffusion.

Furthermore, by analyzing the fiber orientation distribution (FOD) spectrum the LMM provided additional quantification of the orientation information at each length scale. Figure 9 shows the FOD spectrum for a region within the right frontoparietal lobe covering parts of the cingulum, subcallosal and superior occipitofrontal as well as superior longitudinal fasciculus and a region extending from the left thalamus through the internal capsule to the left lentiform nucleus. While the orientation of the restricted diffusion compartments in most GM and WM voxels differed from the hindered diffusion compartments, we generally found a similar orientation distribution for contiguous length scales within the restricted and hindered diffusion regimes, respectively. Obtaining the orientation information at each length scale allowed for a scale-specific tractography. Within the first

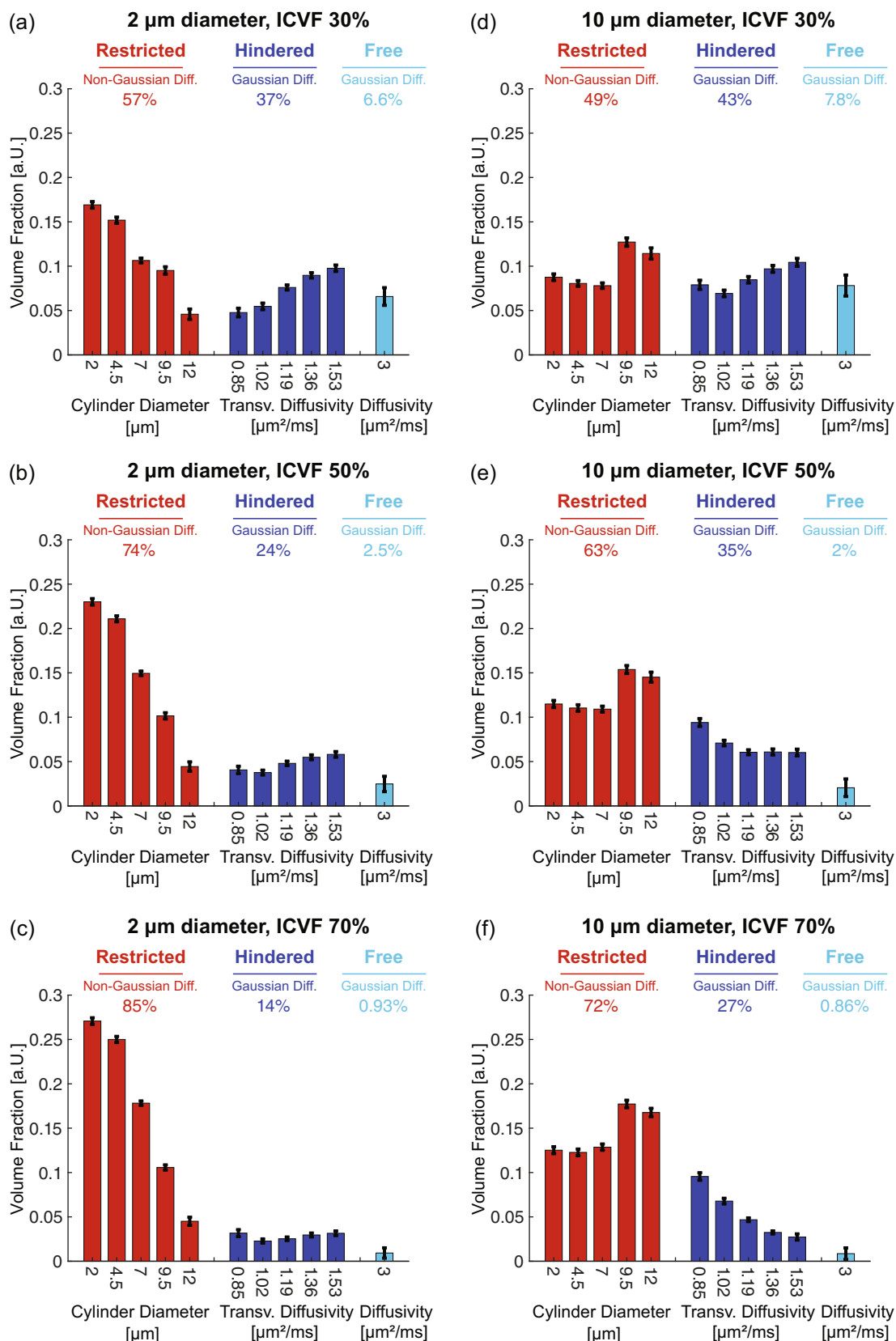


**FIGURE 3** Simulation results: Volume fraction estimation. Shown are exemplary volume fraction estimates of the LMM analysis for a simulated voxel of tightly packed 2  $\mu\text{m}$  ((a)-(c)) and 10  $\mu\text{m}$  ((d)-(f)) impermeable cylinders with an intracellular volume fraction (ICVF) of 30% ((a), (d)), 50% ((b), (e)), and 70% ((c), (f)) and an SNR of 20. Plotted are the mean and standard deviation of 500 different noise realizations. LMM overestimates the fraction of restricted, intracellular, non-Gaussian diffusion. Accuracy increases for larger axon diameters and higher packing densities

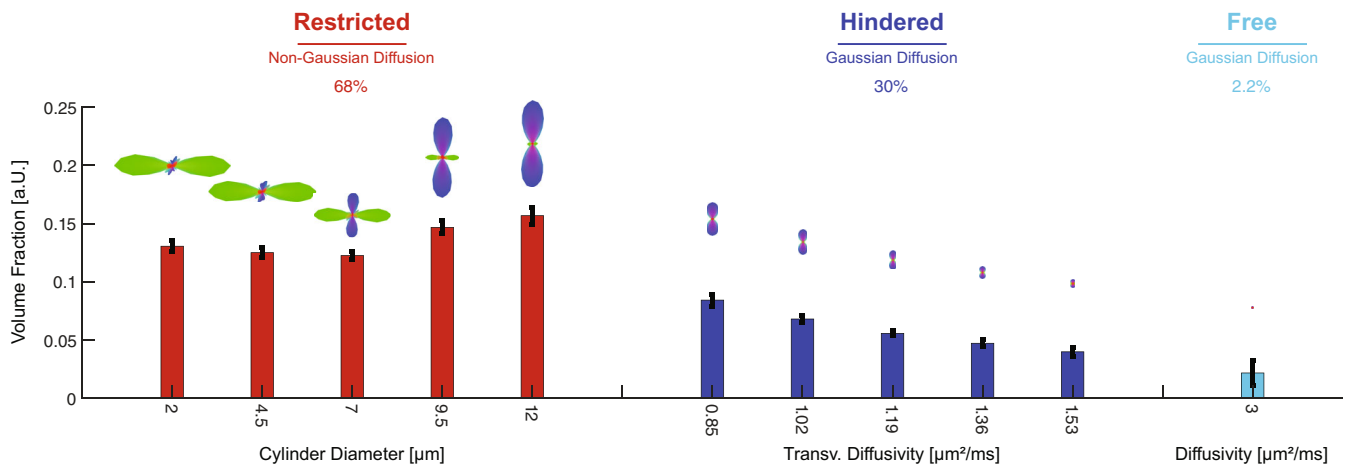


**FIGURE 4** Simulation results: Crossing fibers of different diameters. LMM analysis of a simulated voxel of crossing fibers with an overall intracellular volume fraction of 70% and an SNR of 20. The voxel is composed of 30% horizontal fibers with a diameter of 1 μm and 70% vertical fibers with a diameter of 14 μm. Plotted are the mean and standard deviation of 500 different noise realizations. Shown is the fiber orientation distribution for each length scale. Apart from the previously mentioned cross-talk between adjacent length scales, LMM is able to distinctly separate the orientation distribution of the different sized cylinders

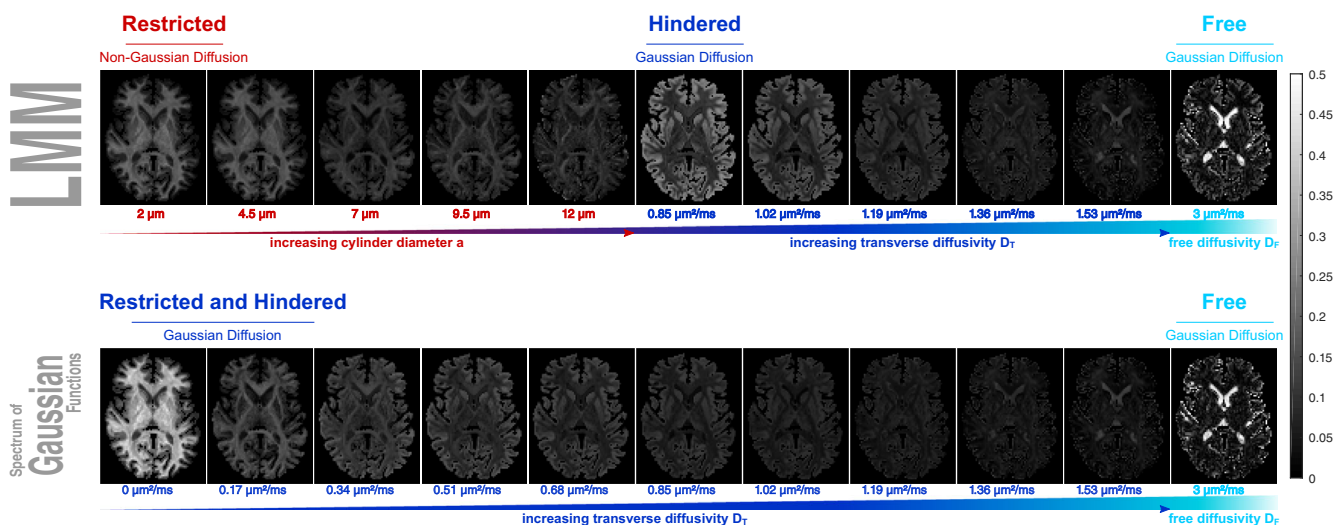


**FIGURE 5** Volume fraction maps. Comparison of the LMM analysis versus an analysis performed for a spectrum of Gaussian functions for in vivo data. Shown are volume fraction maps of an axial slice at the level of the basal ganglia and lateral ventricles with increasing diffusion length scales from left to right. Volume fraction maps are derived from the sum of the ODF values within a voxel, normalized in total to the sum of one. This visualization provides an estimate of the fractional contribution to the total signal per diffusion length scale, with bright voxels indicating a large contribution and dark voxels indicating little or no contribution (see scale)

restricted length scale the path of projection and commissural fibers could be delineated, while short association fibers in the subcortical regions were captured in the first hindered length scale (Figures S1). Furthermore, it was possible to resolve for crossing fibers.

Unlike the approach using a spectrum of Gaussian functions, the LMM explicitly incorporates restricted diffusion in its framework. Utilizing 300 mT/m gradients we were able to probe the regime in which the diffusion signal is sensitive to the finite size of the restricted compartment, such that the LMM could also provide information about the apparent axon diameter. In the group-averaged axon diameter

maps of the LMM analysis, the overall axon diameter size was overestimated, which is a known limitation of axon diameter mapping using currently available gradient strengths up to 300 mT/m (Nilsson et al., 2017). Nevertheless, it was possible to map relative differences in axon diameters. For example, the axon diameter distribution within the corpus callosum reflected known histologic trends of smaller axons in the splenium than the midbody (Aboitiz et al., 1992; Barazany et al., 2009; Veraart et al., 2020) and the corticospinal tract could be delineated by its larger diameter estimates compared with the surrounding tissue (Figure 10). For reference, Figure 10 additionally



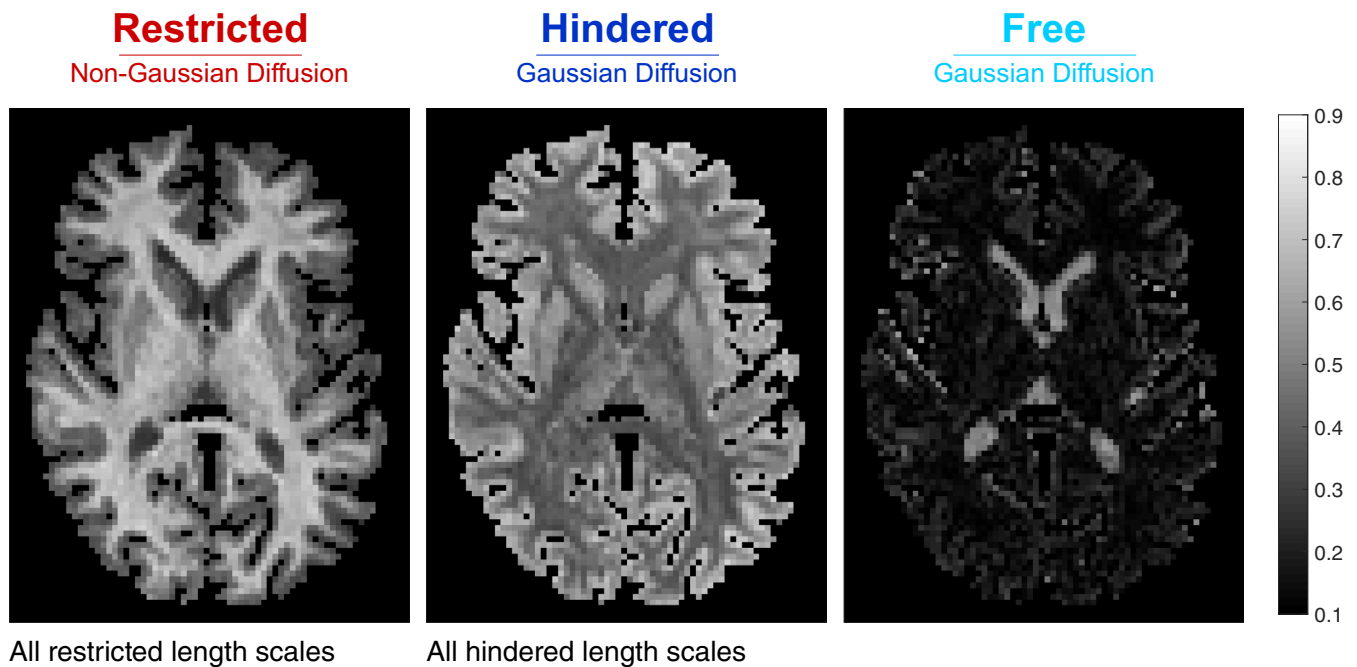


**FIGURE 6** Restricted and hindered volume fraction maps. Volume fraction maps obtained by LMM. These maps comprise the signal from all restricted (left), hindered (middle), and free (right) water compartments. We observe a high fraction of restricted water within the densely packed WM, whereas the cortical GM comprises a high fraction of hindered water diffusion. The free water diffusion signal is exclusively originating from the cerebrospinal fluid spaces. LMM maps depict a high contrast between WM and GM structures

depicts an SMT axon diameter map that also recovers the differences in axon diameters seen in the LMM map.

## 4 | DISCUSSION

The objective of this study was to assess whether extending the Gaussian framework of the original RSI model to include non-Gaussian diffusion response functions in the LMM framework would enable probing the orientational structure of the human brain at multiple length scales with greater specificity for restricted and hindered water compartments. To this end, we acquired a high-quality, comprehensive DW-MRI dataset leveraging state-of-the-art hardware with 300 mT/m gradients and pulse sequence developments. Our results indicate that, to the extent shown in this study, LMM may capture known differences in the degree of restricted diffusion reflecting compartment size in distinct anatomical regions of the brain and that the obtained orientation information at the respective length scales can be potentially used for an enhanced mapping of the human connectome *in vivo*. In comparison to an analysis performed for a spectrum of Gaussian functions, the LMM analysis may offer a refined and more specific representation of WM and GM structures by explicitly modeling of the diffusion behavior in the different tissue compartments. In particular, subtle differences within the restricted diffusion length scales that were evident for the LMM approach could not be captured in an approach using only Gaussian response functions.

As an internal validation, we generated synthetic DW-MRI data using the Monte Carlo diffusion simulator of Camino for diffusion

within impermeable, regularly packed, parallel or crossing cylinders with a range of diameters and intracellular volume fractions. Our simulation results confirm that the estimated microstructural parameters obtained from the LMM analysis are sensitive to known differences in cell/axon size, cellular packing density and intracellular volume fraction within the range of the probed parameters. We further found that the LMM approach provided better separation of the length scales of the restricted water compartments over an approach using a spectrum of Gaussian response functions, indicating that a non-Gaussian diffusion response function is required to capture the DW-MRI signal arising from water molecules diffusing within restricted geometries especially with the high *b*-value data from the Connectome MRI scanner.

It is to note that while the LMM model showed sensitivity to the trends, it did not appear to have good sensitivity to low diameter axons, that is,  $\leq 5 \mu\text{m}$ , as the volume fraction distributions below this limit looked fairly similar. Additionally, LMM consistently overestimated the fraction of intracellular restricted diffusion, particularly for smaller and less tightly packed axon diameters by up to 27%. In contrast to other model-based methods like TractCaliber (Huang et al., 2020) and SMT (Fan et al., 2020), the LMM approach does not assume a single axon diameter but a distribution across length scales. Hence, the estimation task involves more unknown parameters and necessitates solving the linear inverse problem. While approximating compartment sizes is therefore somewhat imprecise, the main advantages of the method are that the inverse operator is linear and provides high computational efficiency as well as the ability to perform exploratory analyses with minimal assumptions about the underlying

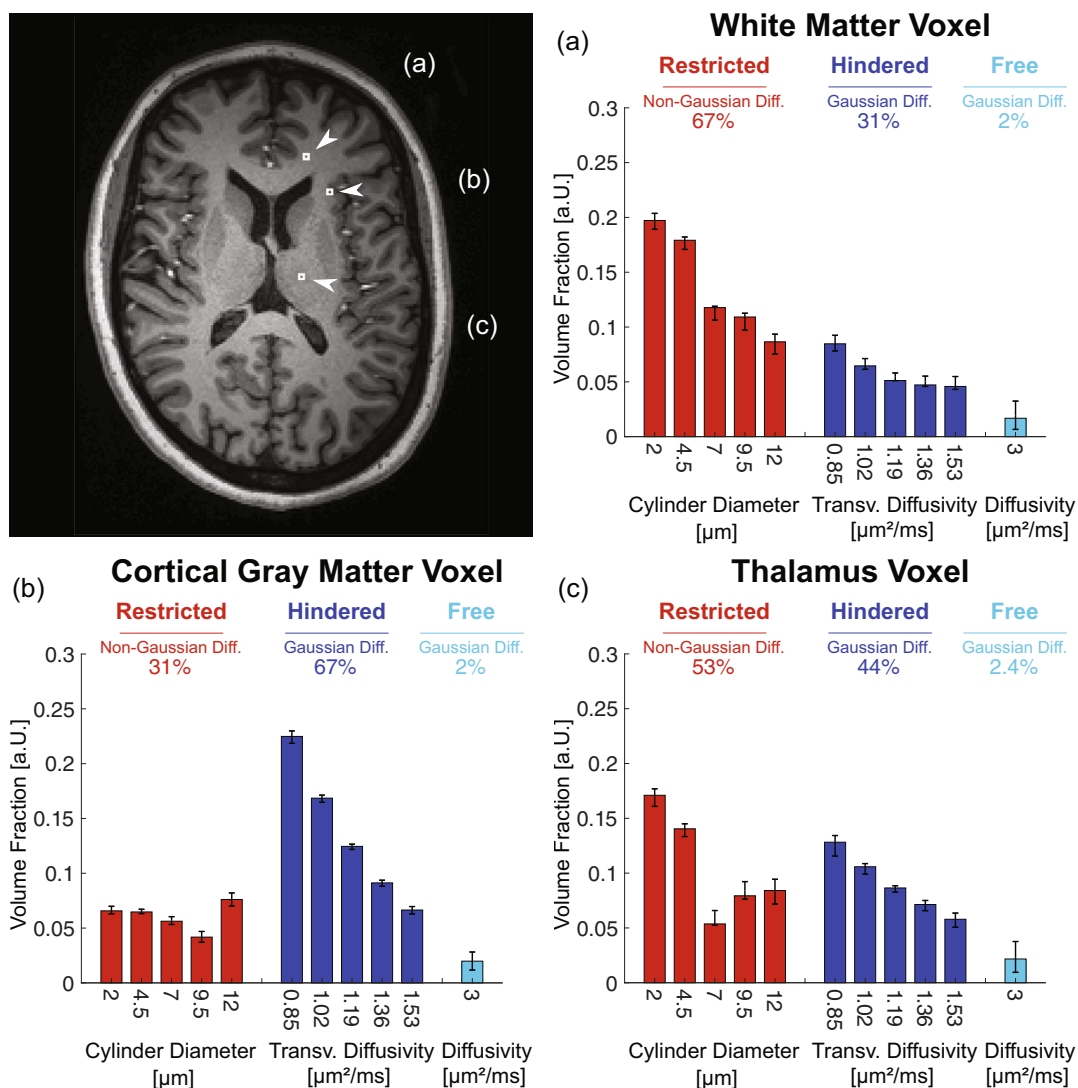


**FIGURE 7** Voxel-wise estimated volume fractions. Representative volume fraction estimates obtained with the LMM analysis for voxels within different WM and GM structures which are consistent with the previously presented volume fraction maps. Within the WM voxel we find a high signal especially originating from the restricted diffusion water compartments (a), whereas the cortical GM voxel shows a high signal originating from the hindered diffusion water length scales (b). The voxel within the thalamus contains a relatively high signal originating from both the restricted and hindered diffusion water compartments, compared with WM and cortical GM (c). Overall, voxel-wise estimated volume fractions of the different sized water compartments are distinguishable between different anatomical structures within the brain. The residual bootstrap is used to calculate the error bars as in (Jeurissen et al., 2011)

tissue microstructure. Assuming infinite SNR, parallel cylinders, and an optimized diffusion encoding scheme, the lower resolution axon diameter limit has been reported to be  $2 \mu\text{m}$  for a maximum diffusion encoding gradient strength of  $300 \text{ mT/m}$  (Drobnjak et al., 2016; Dyrby et al., 2011; Huang et al., 2015; Nilsson et al., 2017). In this study, we used a diffusion acquisition scheme based on a generalized AxCaliber approach that has previously been established to estimate known/expected fiber diameters with a resolution limit of about  $2\text{--}4 \mu\text{m}$  in phantom and in vivo studies (Fan et al., 2018; Fan et al., 2019; Fan et al., 2020; Huang et al., 2015; Huang et al., 2020). Similar to previously published results, our simulation results showed that the larger the diameter and the higher the packing density, the better the sizes of the respective compartments could be

distinguished (Fan et al., 2020). Optimizing the protocol following the guidelines of Drobnjak and Nilsson et al. (Drobnjak et al., 2016; Nilsson et al., 2017) could further improve the model's ability to resolve small compartment sizes.

We observed similar volume fraction estimates and orientation distributions for adjacent length scales within the restricted and hindered water diffusion regime, respectively, suggesting that the individual restricted/hindered length scales cannot be considered completely independent of each other. In particular, our analysis of crossing fibers with distinct cylinder diameters demonstrated the ability of LMM to separate such fiber orientation distributions, however, yielded considerable overlap into adjacent length scales. This type of cross-talk between model parameters was already noted by White

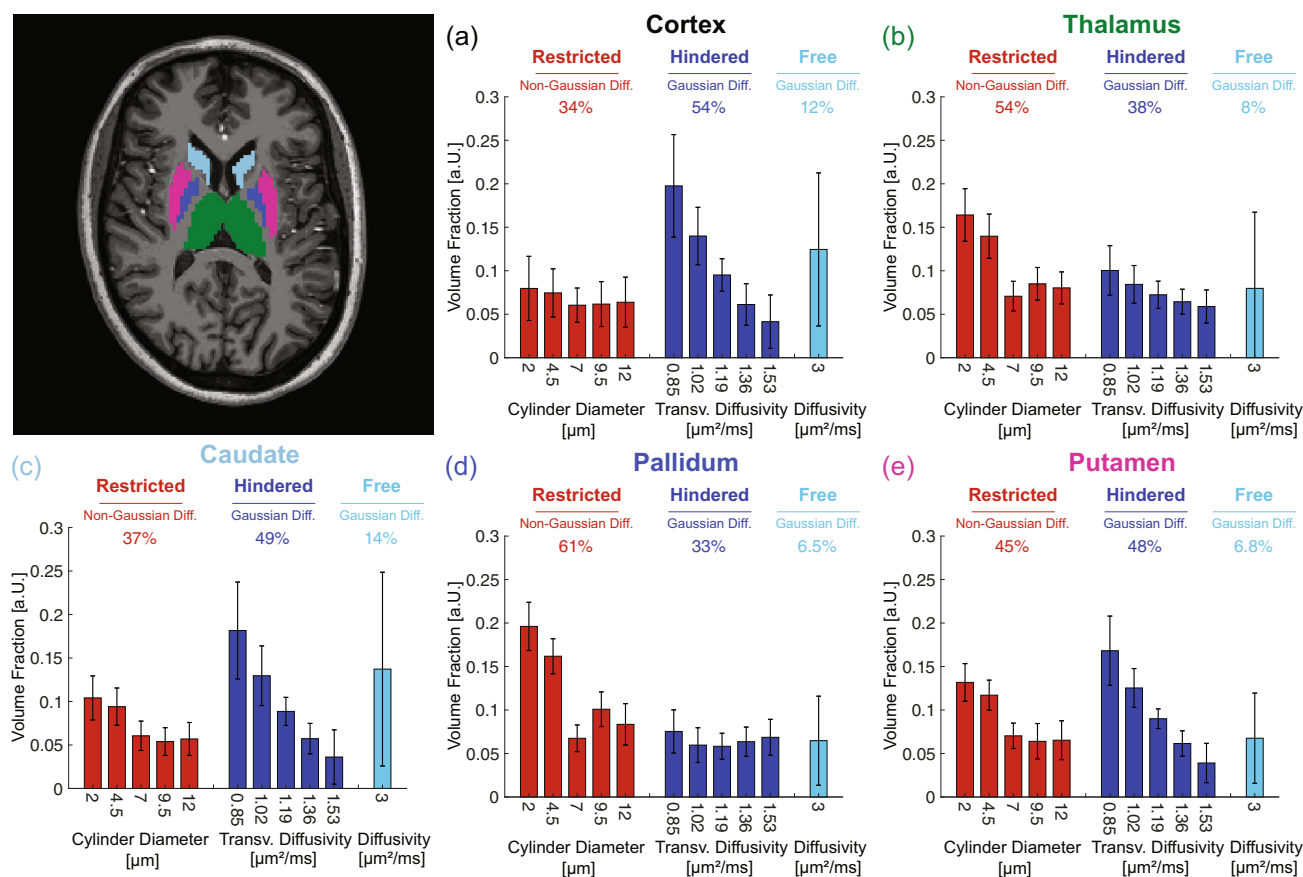


**FIGURE 8** Volume fraction estimates for cortical and deep gray matter structures. Shown are the distributions of volume fractions for different gray matter regions, for the cortex (a), and deep gray matter structures such as the thalamus (b), caudate (c), pallidum (d), and putamen (e). Plotted are the mean and standard deviation for the volume fraction estimates of each length scale within the respective regions. Note the low fraction of restricted and high fraction of hindered diffusion within the cortex. We observe a slight increase of restricted diffusion for the first length scales in the caudate and putamen, whereas these deep gray matter structures retain an almost unchanged high proportion of hindered diffusion. The thalamus and pallidum exhibit a mixture of restricted and hindered diffusion

et al. and further quantified using the concept of the model resolution matrix which allows a characterization of the bias in linear inverse problems (White, Leergaard, et al., 2013a). According to White et al., the intrinsic “scale resolution” of the model is primarily limited by the acquisition protocol and not the model itself or the level of regularization (White, Leergaard, et al., 2013a). Analogous to our findings, they also observed that the level of Tikhonov regularization mainly effects the smoothness of the respective FODs of the different corresponding length scales. Assuming that the slope of the estimated volume fractions over the restricted diffusion length scales matches the simulated axon diameter and intracellular volume fraction one-to-one, in this study we used this monotonic function or calibration curve as a proxy for the average axon diameter in a voxel.

For the empirical data, LMM was able to detect distinct features in the diffusion behavior of different anatomical brain regions and thus differentiate them. First, as expected, we found a high degree of diffusion restriction, particularly within the highly organized, densely packed WM. Considering the cell membrane as the primary contributor to diffusion restriction in biological tissue (White, Leergaard, et al., 2013a), this observation can be attributed to the myelin sheath

of the axons within the WM which allows for little to no exchange between the intra- and extracellular compartments. Second, voxels within the cortical GM showed conversely high volume fraction estimates for the hindered diffusion water compartments, reflecting the differences between GM and WM microstructure. The hindered water DW-MRI signal within the cortex may not only originate from water diffusion within the extracellular compartment, but also from diffusion within glial cells and larger cell bodies which contribute to a large extent to cortical GM tissue (White, Leergaard, et al., 2013a). Following the Einstein equation (see Appendix S1), diffusion occurring within large cell bodies that exceed an upper limit in cell size of 13  $\mu\text{m}$  will be indistinguishable from hindered diffusion and thus will predominantly contribute to the hindered DW-MRI signal, rather than the restricted DW-MRI signal. Furthermore, the much larger permeability of glial cell membranes compared with neuronal cell membranes leads to an increase in diffusivity and exchange between the intra- and extracellular compartment, suggesting a more hindered diffusion within glial cells (Solenov et al., 2004). Third, exemplarily the thalamus, as a deep GM structure, exhibited relatively high volume fraction estimates for both the restricted and hindered length scales,

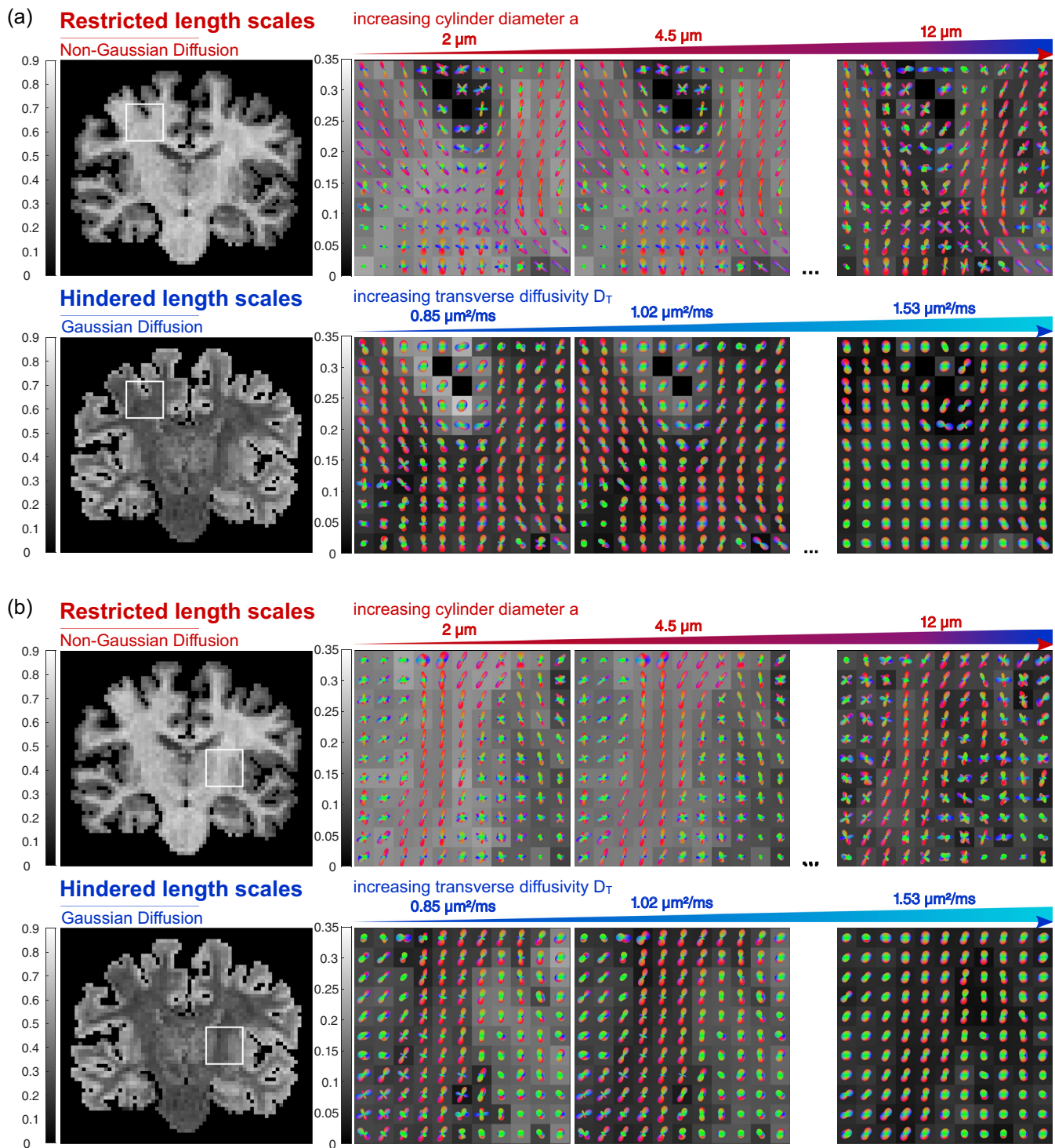


**FIGURE 9** Scale specific fiber orientation distribution. LMM allows computation of scale-specific fiber orientation distributions. Depicted are the normalized fiber orientation distributions of different restricted and hindered diffusion length scales for a region within the right frontoparietal lobe covering parts of the cingulum, subcallosal and superior occipitofrontal as well as superior longitudinal fasciculus (a) and a region extending from the left thalamus through the internal capsule to the left lentiform nucleus (b). The fiber orientation distributions were overlaid with their corresponding volume fractions as gray values in each voxel. Note the different fiber orientation distributions in the restricted versus hindered diffusion regime within the subcortical region and the internal capsule

indicating some degree of additional restriction compared with cortical GM. Dissimilar to other subcortical GM structures, the thalamus comprises unmyelinated and myelinated nerve fibers (Wiegell

et al., 2003). The latter, also referred to as the thalamocortical striations, have already been shown to provide sufficient diffusion restriction to be examined with diffusion tensor imaging and which we thus



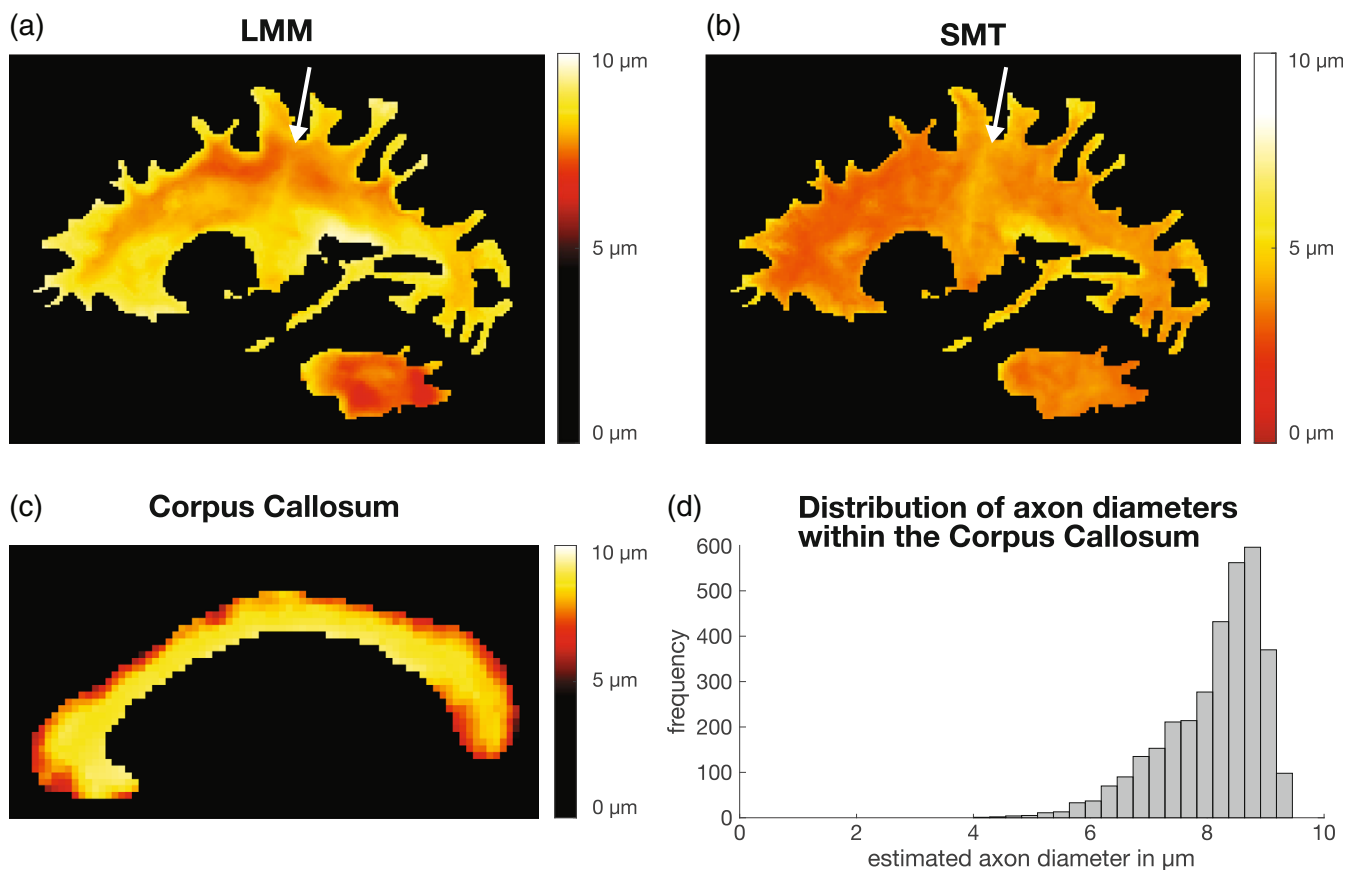


**FIGURE 10** Group-averaged axon diameter maps. Group-averaged maps of axon diameter estimates across 15 healthy subjects. Shown is a sagittal slice through the left corticospinal tract (denoted with a white arrow), obtained using the LMM (a) versus SMT (b) approach. While the overall axon diameter is overestimated by the LMM in comparison to the SMT, it was possible to map the overall trends of axon diameters by the LMM, for example, the corticospinal tract with its larger diameters was distinguishable from its surrounding tissue. (c) Depicts the estimated axon diameters within a mid-sagittal slice at the corpus callosum and (d) the distribution of axon diameter estimates within the corpus callosum. Although axon diameters in the corpus callosum are overestimated, LMM was able to recover known histologic trends of smaller axons in the splenium than the midbody of the corpus callosum

argue contribute to the higher volume fraction estimates for the restricted water compartments in our model (Wiegell et al., 2003). Similarly, LMM analysis of the globus pallidus yielded a high proportion of restricted diffusion, whose pale appearance is attributed to myelinated axons (Latin pallidus translates to pale) (Javed & Cascella, 2022). This contrasts with the unmyelinated structures, that is, putamen and caudate, which appear darker and exhibited a correspondingly lower fraction of restricted and a high fraction of hindered diffusion comparable to the cortex (Javed & Cascella, 2022). Compared with equivalent volume fraction maps obtained with an analysis using only Gaussian diffusion response functions, our results suggest that the LMM analysis preserves the differences in diffusion behavior between WM and GM more accurately. More specifically, in contrast to the LMM approach, small differences within the restricted diffusion length scales could not be captured by a spectrum of only Gaussian diffusion response functions as the restricted diffusion information is subsumed in the first(s) length scale(s).

By separating orientation distributions of restricted and hindered diffusion water compartments over a range of length scales, the LMM

method may provide a more specific probe of neural architecture for quantifying and mapping the connectome in vivo. We found a dissimilar orientation distribution in GM and WM voxels for the restricted and hindered water diffusion length scales, respectively. In particular within the subcortical regions, we were able to delineate many short association fibers that connect adjacent gyri within the first hindered length scale, while the course of projection and commissural fibers was reflected in particular within the first restricted length scales (Meynert & Sachs, 1885). Using spherical deconvolution with tissue-specific response functions and multi-shell DW-MRI data, de Luca et al. were able to show that such a framework can be used to improve the FOD estimation within the cortical GM paving the way to GM fiber tractography (de Luca et al., 2020).

In contrast to the analysis performed for a spectrum of Gaussian diffusion functions, the LMM method explicitly incorporates a diffusion model within impermeable cylinders of increasing diameter in its framework. Assuming that the slope of the estimated volume fractions over these restricted length scales can be utilized as a proxy for the average axon diameter in a voxel, the LMM method facilitates the

computation of “apparent axon diameter maps” in vivo. Such maps provide condensed information about relative axonal size throughout the brain, and the LMM-based results exhibited consistent trends across all 16 healthy subjects. The obtained group-averaged axon diameter maps yielded concordant differences in histologically known tissue microstructural properties. For instance, we found that axons in the corticospinal tracts feature among the largest diameters of axons in the human brain ( $\sim 1 \mu\text{m}$  larger compared with surrounding WM), which is substantiated by previous histological studies in humans (Graf von Keyserlingk & Schramm, 1984). Furthermore, LMM was able to recover known histologic trends of larger axons in the midbody than the splenium of the corpus callosum, but did not fully recover the trend of smaller axons in the genu of the corpus callosum (Aboitiz et al., 1992; Barazany et al., 2009; Veraart et al., 2020). Despite consistent trends with histology, we should note that the reported diameter values ( $\geq 5 \mu\text{m}$  in the whole brain) overestimate the majority of axon diameters in the human brain by almost an order of magnitude. Most axon diameters within the human brain range from 0.1 up to 10  $\mu\text{m}$  and lay within the cell size range that we are able to probe with our acquisition protocol (Assaf et al., 2013). However, as already stated above, axons smaller than  $\sim 2 \mu\text{m}$  remain below the diffusion resolution limit at 300 mT/m (Drobnjak et al., 2016; Dyrby et al., 2011; Huang et al., 2015; Nilsson et al., 2017). Furthermore, employing a single axon diameter to subsume the average compartment size skews the estimate towards larger diameter axons, whose larger water content contributes to the overall decay of the diffusion signal to a greater extent than the lesser water content of smaller, more restricted axons (Alexander et al., 2010). Though significantly overestimating the axon diameter, the LMM group-averaged axon diameter maps recovered similar trends as axon diameter maps obtained using an SMT analysis.

While our results cannot be considered as fully quantitative measures of axon diameter and density, the derived maps can be thought of as axon diameter- and volume fraction-weighted images similarly to (Huang et al., 2020), that appear to be sensitive to underlying microstructural features of tissue and capture general trends in axon size and packing density. The precise relationship between tissue microstructure, diffusion signal, and parameters estimated by LMM needs further investigation, which is alleviated by the availability of high diffusion gradient strengths for in vivo imaging with the ongoing development of the next-generation “Connectome 2.0” scanner technology (Huang et al., 2021). The advent of higher gradient strengths on human MRI scanners has captured the interest of neuroscientists, as high gradients may enable “in vivo histology,” that is, the possibility of probing tissue microstructure in the living human brain, as exemplified through axon diameter mapping. Tracking axonal pathology non-invasively in white matter disorders such as multiple sclerosis (de Santis et al., 2019; Huang et al., 2016; Huang et al., 2019) and aging (Fan et al., 2019) using high-gradient DW-MRI may enable the assessment of axonal damage in patients as they experience progression of disease and disability. Scanners such as MAGNUS (Foo et al., 2020) and Connectome systems (Jones et al., 2018; McNab et al., 2013) are becoming increasingly mainstream and are paving the

way to higher gradient strengths on clinical systems, thereby enabling such capabilities as axon diameter mapping and other tissue microstructural imaging techniques to be performed on clinically available scanners.

The LMM method extends the Gaussian framework of the original RSI model to include non-Gaussian diffusion response functions. As such, it gains greater specificity to restricted and hindered water compartments compared with RSI while offering a general framework for probing the size and orientational structure of human GM and WM, in states of health and disease. We emphasize that the LMM drives at tissue microstructure without imposing assumptions about the composition of the tissue, which is a limitation of many biophysical models. The LMM can thus be applied to healthy tissue as well as pathology. In comparison to the original RSI approach, we used a general framework that imposes few assumptions on the underlying tissue microstructure (Le Bihan, 1995) and preserves the advantages of the RSI approach in its linear implementation, which is computationally efficient. As such, LMM characterizes diffusion within human brain tissue as basically occurring in three compartments: (i) restricted diffusion within intracellular compartments, modeled as diffusion within impermeable cylinders of different diameters, (ii) hindered diffusion in extracellular compartments, modeled with an anisotropic, cylindrically symmetric diffusion tensor with fixed longitudinal and varying transverse diffusivities, and (iii) free, isotropic diffusion in CSF. Panagiotaki et al. (Panagiotaki et al., 2012) and Ferizi et al. (Ferizi et al., 2014) have shown that three compartment models, designed to capture extracellular diffusion, intra-axonal diffusion, and isotropically restricted diffusion as in glial cells, best fit the DW-MRI data from human brain WM. They demonstrated that the anisotropic cylindrically symmetric diffusion tensor used in our model best represents the DW-MRI signal arising from the extracellular compartment and that the impermeable cylinder of non-zero diameter provides a reasonable model to first order for describing water diffusion within axons. Furthermore, they showed that spherical cellular structures, such as glial cells, even though best captured with a dot or a sphere, can also be well captured with isotropically oriented impermeable cylinders of non-zero diameter (Panagiotaki et al., 2012). Depending on the field of research or application, these model assumptions can be further adapted, for example, to represent nodular structures with spheres of different diameter (Palombo et al., 2020), to consider effects of permeability (Solenov et al., 2004) or the diffusion time dependency of the signal within extracellular water compartments (Burcaw et al., 2015; Lee et al., 2018).

A central feature of many inverse problems is they can be “ill-posed”, meaning that the solution may not be unique and/or show numerical instabilities that result in noise amplification. To make the inverse problem at hand more well-behaved, we used a multi-shell, multi-diffusion time acquisition scheme versus a Cartesian q-space sampling scheme as originally utilized in the RSI approach (White, Leergaard, et al., 2013a). This allowed us to use a spherical deconvolution approach in both the signal as well as the FOD space to improve the numerical conditioning of the inverse operator. Nevertheless, in light of the large number of unknown parameters, we solved the



multi-scale, linear inverse problem using standard least squares estimation with Tikhonov regularization to help prevent overfitting/noise amplification, resulting in robust estimates of the volume fractions for different length scales and the associated FODs. However, we should note that the very general framework of the LMM allows FODs in principle to be different across different restricted length scales. To further reduce the effective number of parameters to be estimated, we could add further constraints. For example, the adjacent length scales within the same compartment (restricted vs. hindered) could be assumed a priori to have more similar FODs or in the limiting case assume that all restricted/hindered length scales are associated with a single FOD.

For the differentiation and estimation of compartment sizes, we recommend the use of at least two diffusion times (Huang et al., 2015). The use of multi-diffusion time data has been used in our previous studies (Huang et al., 2015; Huang et al., 2020) and others' (de Santis et al., 2016; Harkins et al., 2021) to map axonal diameter using DW-MRI. Nonetheless, we acknowledge that the LMM approach could also be applied to multi-shell data acquired with a single diffusion time, recognizing that the sensitivity to length scales across restricted and hindered compartments may be more limited. For the analysis of data acquired with nonspherical sampling, either Cartesian sampling or due to gradient nonlinearities, the single-fiber response functions could be adopted to also describe their radial dependency, similar to (Morez et al., 2021).

Using conventional MRI gradient systems, the RSI approach has already shown great promise in addressing key clinical challenges in neuro-oncology, such as improved tumor conspicuity, differentiation between treatment response and pseudo-response, delineation of WM pathways within peritumoral edema, and risk stratification in cancer patients (Latysheva et al., 2020; McDonald et al., 2016; White et al., 2014; White, McDonald, et al., 2013b). Our results indicate that accounting for non-Gaussian diffusion in the extended framework of LMM increases sensitivity to restricted diffusion within confined cellular structures. When used in conjunction with optimized pulse sequences and state-of-the-art diffusion encoding gradient hardware, the LMM approach can enable more precise characterization/targeting of lesions for the development of tissue signatures particularly within tumorous tissue environments (Nilsson et al., 2018) possibly opening new avenues for therapy planning, including radiotherapy and surgical resection. Further studies will focus on implementing the LMM approach in a clinical setting.

## 5 | CONCLUSION

In this study, we present a general analysis approach for DW-MRI data, that extends the RSI framework to represent restricted water compartments with non-Gaussian response functions. The LMM retains the advantages of the RSI approach in its implementation as a linear inverse problem, while incorporating a more realistic model for restricted diffusion. When combined with cutting-edge acquisition techniques, the LMM framework offers a powerful analysis method for separating orientation distributions of restricted and hindered

diffusion water compartments over a range of length scales. Thereby, LMM allows for a more detailed characterization of tissue microstructure with greater specificity to diffusion in intra- and extracellular compartments. Consistency between our results and previously published histological data is encouraging and indicates that our measurements are sensitive to particular microstructural tissue features of different regions within the brain. The estimation of restricted and hindered volume fractions and compartment sizes may enable the development of distinct diffusion microstructural signatures of healthy and diseased tissue, while orientation distribution information at different length scales could give additional information about the brain's microscopic structure and provide a roadmap for improved radiation oncology and surgical planning.

## ACKNOWLEDGMENT

Open Access funding enabled and organized by Projekt DEAL.

## FUNDING INFORMATION

This work was supported by the National Institutes of Health (grant numbers U01-EB026996, P41-EB030006, K23-NS096056, P41-EB017183, R01-NS118187, R00EB015445, R01MH111829) and the National Natural Science Foundation of China (NSFC 82071994).

## CONFLICT OF INTEREST

It is to specifically state that no competing interests are at stake and there is no conflict of interest with other people or organizations that could inappropriately influence or bias the content of the paper.

## DATA AVAILABILITY STATEMENT

The LMM algorithm is available in the article's supplementary material. MRI datasets that can be used for LMM analysis have been made publicly available through the figshare repository (Tian et al., 2022): [https://springernature.figshare.com/collections/Comprehensive\\_diffusion\\_MRI\\_dataset\\_for\\_in\\_vivo\\_human\\_brain\\_microstructure\\_mapping\\_using\\_300\\_mT\\_m\\_gradients/5315474](https://springernature.figshare.com/collections/Comprehensive_diffusion_MRI_dataset_for_in_vivo_human_brain_microstructure_mapping_using_300_mT_m_gradients/5315474).

## ORCID

Barbara D. Wichtmann  <https://orcid.org/0000-0001-8020-0202>

Qiuyun Fan  <https://orcid.org/0000-0001-9053-6279>

## REFERENCES

- Aboitiz, F., Scheibel, A. B., Fisher, R. S., & Zaidel, E. (1992). Fiber composition of the human corpus callosum. *Brain Research*, 598(1–2), 143–153. [https://doi.org/10.1016/0006-8993\(92\)90178-c](https://doi.org/10.1016/0006-8993(92)90178-c)
- Afzali, M., Nilsson, M., Palombo, M., & Jones, D. K. (2021). Spheriously? The challenges of estimating sphere radius non-invasively in the human brain from diffusion MRI. *NeuroImage*, 237, 118183. <https://doi.org/10.1016/j.neuroimage.2021.118183>
- Alexander, D. C. (2008). A general framework for experiment design in diffusion MRI and its application in measuring direct tissue-microstructure features. *Magnetic Resonance in Medicine*, 60(2), 439–448. <https://doi.org/10.1002/mrm.21646>
- Alexander, D. C., Dyrby, T. B., Nilsson, M., & Zhang, H. (2019). Imaging brain microstructure with diffusion MRI: Practicality and applications. *NMR in Biomedicine*, 32(4), e3841. <https://doi.org/10.1002/nbm.3841>

- Alexander, D. C., Hubbard, P. L., Hall, M. G., Moore, E. A., Ptito, M., Parker, G. J., & Dyrby, T. B. (2010). Orientationally invariant indices of axon diameter and density from diffusion MRI. *NeuroImage*, 52(4), 1374–1389. <https://doi.org/10.1016/j.neuroimage.2010.05.043>
- Andersson, J. L., Skare, S., & Ashburner, J. (2003). How to correct susceptibility distortions in spin-echo echo-planar images: Application to diffusion tensor imaging. *NeuroImage*, 20(2), 870–888. [https://doi.org/10.1016/S1053-8119\(03\)00336-7](https://doi.org/10.1016/S1053-8119(03)00336-7)
- Andersson, J. L., & Sotiropoulos, S. N. (2015). Non-parametric representation and prediction of single- and multi-shell diffusion-weighted MRI data using Gaussian processes. *NeuroImage*, 122, 166–176. <https://doi.org/10.1016/j.neuroimage.2015.07.067>
- Andersson, J. L. R., Graham, M. S., Zsoldos, E., & Sotiropoulos, S. N. (2016). Incorporating outlier detection and replacement into a non-parametric framework for movement and distortion correction of diffusion MR images. *NeuroImage*, 141, 556–572. <https://doi.org/10.1016/j.neuroimage.2016.06.058>
- Andersson, J. L. R., & Sotiropoulos, S. N. (2016). An integrated approach to correction for off-resonance effects and subject movement in diffusion MR imaging. *NeuroImage*, 125, 1063–1078. <https://doi.org/10.1016/j.neuroimage.2015.10.019>
- Assaf, Y., Alexander, D. C., Jones, D. K., Bizzi, A., Behrens, T. E., Clark, C. A., Cohen, Y., Dyrby, T. B., Huppi, P. S., Knoesche, T. R., LeBihan, D., Parker, G. J. M., Poupon, C., CONNECT Consortium, Anaby, D., Anwender, A., Bar, L., Barazany, D., Blumenfeld-Katzir, T., ... Zhou, F. L. (2013). The CONNECT project: Combining macro- and micro-structure. *NeuroImage*, 80, 273–282. <https://doi.org/10.1016/j.neuroimage.2013.05.055>
- Assaf, Y., & Basser, P. J. (2005). Composite hindered and restricted model of diffusion (CHARMED) MR imaging of the human brain. *NeuroImage*, 27(1), 48–58. <https://doi.org/10.1016/j.neuroimage.2005.03.042>
- Assaf, Y., Blumenfeld-Katzir, T., Yovel, Y., & Basser, P. J. (2008). AxCaliber: A method for measuring axon diameter distribution from diffusion MRI. *Magnetic Resonance in Medicine*, 59(6), 1347–1354. <https://doi.org/10.1002/mrm.21577>
- Barazany, D., Basser, P. J., & Assaf, Y. (2009). In vivo measurement of axon diameter distribution in the corpus callosum of rat brain. *Brain*, 132, 1210–1220. <https://doi.org/10.1093/brain/awp042>
- Basser, P. J., Mattiello, J., & LeBihan, D. (1994). Estimation of the effective self-diffusion tensor from the NMR spin echo. *Journal of Magnetic Resonance. Series B*, 103(3), 247–254. <https://doi.org/10.1006/jmrb.1994.1037>
- Burcaw, L. M., Fieremans, E., & Novikov, D. S. (2015). Mesoscopic structure of neuronal tracts from time-dependent diffusion. *NeuroImage*, 114, 18–37. <https://doi.org/10.1016/j.neuroimage.2015.03.061>
- Callaghan, P. T. (1993). *Principles of nuclear magnetic resonance microscopy*. Oxford University Press on Demand.
- Callaghan, P. T., & Stepisnik, J. (1995). Spatially-distributed pulsed gradient spin echo NMR using single-wire proximity. *Physical Review Letters*, 75(24), 4532–4535. <https://doi.org/10.1103/PhysRevLett.75.4532>
- Cook, P. A., Bai, Y., Nedjati-Gilani, S., Seunarine, K. K., Hall, M. G., Parker, G. J. M., & Alexander, D. C. (2006). Camino: Open-source diffusion-MRI reconstruction and processing. Paper presented at the 14th scientific meeting of the International Society for Magnetic Resonance in medicine, Seattle WA, USA.
- de Luca, A., Guo, F., Froeling, M., & Leemans, A. (2020). Spherical deconvolution with tissue-specific response functions and multi-shell diffusion MRI to estimate multiple fiber orientation distributions (mFODs). *NeuroImage*, 222, 117206. <https://doi.org/10.1016/j.neuroimage.2020.117206>
- de Santis, S., Herranz, E., Treaba, C. A., Barletta, V., Mehndiratta, A., Mainero, C., & Toschi, N. (2019). Whole brain in vivo axonal diameter mapping in multiple sclerosis. *Annual International Conference of the IEEE Engineering in Medicine and Biology Society*, 2019, 204–207. <https://doi.org/10.1109/EMBC.2019.8856433>
- de Santis, S., Jones, D. K., & Roebroeck, A. (2016). Including diffusion time dependence in the extra-axonal space improves in vivo estimates of axonal diameter and density in human white matter. *NeuroImage*, 130, 91–103. <https://doi.org/10.1016/j.neuroimage.2016.01.047>
- Descoteaux, M., Angelino, E., Fitzgibbons, S., & Deriche, R. (2007). Regularized, fast, and robust analytical Q-ball imaging. *Magnetic Resonance in Medicine*, 58(3), 497–510. <https://doi.org/10.1002/mrm.21277>
- Drobnjak, I., Zhang, H., Ianus, A., Kaden, E., & Alexander, D. C. (2016). PGSE, OGSE, and sensitivity to axon diameter in diffusion MRI: Insight from a simulation study. *Magnetic Resonance in Medicine*, 75(2), 688–700. <https://doi.org/10.1002/mrm.25631>
- Duval, T., Stikov, N., & Cohen-Adad, J. (2016). Modeling white matter microstructure. *Functional Neurology*, 31(4), 217–228. <https://doi.org/10.11138/fneur/2016.31.4.217>
- Dyrby, T. B., Baare, W. F., Alexander, D. C., Jelsing, J., Garde, E., & Sogaard, L. V. (2011). An ex vivo imaging pipeline for producing high-quality and high-resolution diffusion-weighted imaging datasets. *Human Brain Mapping*, 32(4), 544–563. <https://doi.org/10.1002/hbm.21043>
- Eichner, C., Cauley, S. F., Cohen-Adad, J., Moller, H. E., Turner, R., Setsompop, K., & Wald, L. L. (2015). Real diffusion-weighted MRI enabling true signal averaging and increased diffusion contrast. *NeuroImage*, 122, 373–384. <https://doi.org/10.1016/j.neuroimage.2015.07.074>
- Fan, Q., Nummenmaa, A., Wichtmann, B., Witzel, T., Mekkaoui, C., Schneider, W., Wald, L. L., & Huang, S. Y. (2018). Validation of diffusion MRI estimates of compartment size and volume fraction in a biomimetic brain phantom using a human MRI scanner with 300 mT/m maximum gradient strength. *NeuroImage*, 182, 469–478. <https://doi.org/10.1016/j.neuroimage.2018.01.004>
- Fan, Q., Nummenmaa, A., Witzel, T., Ohringer, N., Tian, Q., Setsompop, K., Klawiter, E. C., Rosen, B. R., Wald, L. L., Huang, S. Y., & Huang, S. Y. (2020). Axon diameter index estimation independent of fiber orientation distribution using high-gradient diffusion MRI. *NeuroImage*, 222, 117197. <https://doi.org/10.1016/j.neuroimage.2020.117197>
- Fan, Q., Nummenmaa, A., Witzel, T., Zanzonico, R., Keil, B., Cauley, S., Polimeni, J. R., Tisdall, D., van Dijk, K. R. A., Buckner, R. L., Wedeen, V. J., Rosen, B. R., & Wald, L. L. (2014). Investigating the capability to resolve complex white matter structures with high b-value diffusion magnetic resonance imaging on the MGH-USC Connectom scanner. *Brain Connectivity*, 4(9), 718–726. <https://doi.org/10.1089/brain.2014.0305>
- Fan, Q., Polackal, M. N., Tian, Q., Ngamsombat, C., Nummenmaa, A., Witzel, T., Klawiter, E. C., & Huang, S. Y. (2021). Scan-rescan repeatability of axonal imaging metrics using high-gradient diffusion MRI and statistical implications for study design. *NeuroImage*, 240, 118323. <https://doi.org/10.1016/j.neuroimage.2021.118323>
- Fan, Q., Tian, Q., Ohringer, N. A., Nummenmaa, A., Witzel, T., Tobbyne, S. M., Klawiter, E. C., Mekkaoui, C., Rosen, B. R., Wald, L. L., Salat, D. H., & Huang, S. Y. (2019). Age-related alterations in axonal microstructure in the corpus callosum measured by high-gradient diffusion MRI. *NeuroImage*, 191, 325–336. <https://doi.org/10.1016/j.neuroimage.2019.02.036>
- Fan, Q., Witzel, T., Nummenmaa, A., van Dijk, K. R., van Horn, J. D., Drews, M. K., Somerville, L. H., Sheridan, M. A., Santillana, R. M., Snyder, J., Hedden, T., Shaw, E. E., Hollinshead, M. O., Renvall, V., Zanzonico, R., Keil, B., Cauley, S., Polimeni, J. R., Tisdall, D., ... Rosen, B. R. (2016). MGH-USC human connectome project datasets with ultra-high b-value diffusion MRI. *NeuroImage*, 124, 1108–1114. <https://doi.org/10.1016/j.neuroimage.2015.08.075>
- Feinberg, D. A., Moeller, S., Smith, S. M., Auerbach, E., Ramanna, S., Gunther, M., Glasser, M. F., Miller, K. L., Ugurbil, K., Yacoub, E., & Yacoub, E. (2010). Multiplexed echo planar imaging for sub-second whole brain fMRI and fast diffusion imaging. *PLoS One*, 5(12), e15710. <https://doi.org/10.1371/journal.pone.0015710>

- Feinberg, D. A., & Setsompop, K. (2013). Ultra-fast MRI of the human brain with simultaneous multi-slice imaging. *Journal of Magnetic Resonance*, 229, 90–100. <https://doi.org/10.1016/j.jmr.2013.02.002>
- Ferizi, U., Schneider, T., Panagiotaki, E., Nedjati-Gilani, G., Zhang, H., Wheeler-Kingshott, C. A., & Alexander, D. C. (2014). A ranking of diffusion MRI compartment models with in vivo human brain data. *Magnetic Resonance in Medicine*, 72(6), 1785–1792. <https://doi.org/10.1002/mrm.25080>
- Fischl, B., Salat, D. H., Busa, E., Albert, M., Dieterich, M., Haselgrove, C., van der Kouwe, A., Killiany, R., Kennedy, D., Klaveness, S., Montillo, A., Makris, N., Rosen, B., & Dale, A. M. (2002). Whole brain segmentation: Automated labeling of neuroanatomical structures in the human brain. *Neuron*, 33(3), 341–355.
- Foo, T. K. F., Tan, E. T., Vermilyea, M. E., Hua, Y., Fiveland, E. W., Piel, J. E., Park, K., Ricci, J., Thompson, P. S., Graziani, D., Conte, G., Kagan, A., Bai, Y., Vasil, C., Tarasek, M., Yeo, D. T., Snell, F., Lee, D., Dean, A., ... Ho, V. B. (2020). Highly efficient head-only magnetic field insert gradient coil for achieving simultaneous high gradient amplitude and slew rate at 3.0T (MAGNUS) for brain microstructure imaging. *Magnetic Resonance in Medicine*, 83(6), 2356–2369. <https://doi.org/10.1002/mrm.28087>
- Glasser, M. F., Sotiropoulos, S. N., Wilson, J. A., Coalson, T. S., Fischl, B., Andersson, J. L., Xu, J., Jbabdi, S., Webster, M., Polimeni, J. R., van Essen, D. C., Jenkinson, M., & Consortium, W. U.-M. H. (2013). The minimal preprocessing pipelines for the human connectome project. *NeuroImage*, 80, 105–124. <https://doi.org/10.1016/j.neuroimage.2013.04.127>
- von Keyserlingk, D. G., & Schramm, U. (1984). Diameter of axons and thickness of myelin sheaths of the pyramidal tract fibres in the adult human medullary pyramid. *Anatomischer Anzeiger*, 157(2), 97–111.
- Greve, D. N., & Fischl, B. (2009). Accurate and robust brain image alignment using boundary-based registration. *NeuroImage*, 48(1), 63–72. <https://doi.org/10.1016/j.neuroimage.2009.06.060>
- Hall, M. G., & Alexander, D. C. (2009). Convergence and parameter choice for Monte-Carlo simulations of diffusion MRI. *IEEE Transactions on Medical Imaging*, 28(9), 1354–1364. <https://doi.org/10.1109/TMI.2009.2015756>
- Harkins, K. D., Beaulieu, C., Xu, J., Gore, J. C., & Does, M. D. (2021). A simple estimate of axon size with diffusion MRI. *NeuroImage*, 227, 117619. <https://doi.org/10.1016/j.neuroimage.2020.117619>
- Harms, R. L., Fritz, F. J., Tobisch, A., Goebel, R., & Roebroeck, A. (2017). Robust and fast nonlinear optimization of diffusion MRI microstructure models. *NeuroImage*, 155, 82–96. <https://doi.org/10.1016/j.neuroimage.2017.04.064>
- Henriques, R. N., Palombo, M., Jespersen, S. N., Shemesh, N., Lundell, H., & Ianus, A. (2021). Double diffusion encoding and applications for biomedical imaging. *Journal of Neuroscience Methods*, 348, 108989. <https://doi.org/10.1016/j.jneumeth.2020.108989>
- Huang, S. Y., Fan, Q., Machado, N., Eloyan, A., Bireley, J. D., Russo, A. W., Tobyne, S. M., Patel, K. R., Brewer, K., Rapaport, S. F., Nummenmaa, A., Witzel, T., Sherman, J. C., Wald, L. L., & Klawiter, E. C. (2019). Corpus callosum axon diameter relates to cognitive impairment in multiple sclerosis. *Annals of Clinical Translational Neurology*, 6(5), 882–892. <https://doi.org/10.1002/acn3.760>
- Huang, S. Y., Nummenmaa, A., Witzel, T., Duval, T., Cohen-Adad, J., Wald, L. L., & McNab, J. A. (2015). The impact of gradient strength on in vivo diffusion MRI estimates of axon diameter. *NeuroImage*, 106, 464–472. <https://doi.org/10.1016/j.neuroimage.2014.12.008>
- Huang, S. Y., Tian, Q., Fan, Q., Witzel, T., Wichtmann, B., McNab, J. A., Bireley, J. D., Machado, N., Klawiter, E. C., Mekkaoui, C., Wald, L. L., Nummenmaa, A., & Nummenmaa, A. (2020). High-gradient diffusion MRI reveals distinct estimates of axon diameter index within different white matter tracts in the in vivo human brain. *Brain Structure & Function*, 225(4), 1277–1291. <https://doi.org/10.1007/s00429-019-01961-2>
- Huang, S. Y., Tobyne, S. M., Nummenmaa, A., Witzel, T., Wald, L. L., McNab, J. A., & Klawiter, E. C. (2016). Characterization of axonal disease in patients with multiple sclerosis using high-gradient-diffusion MR imaging. *Radiology*, 280(1), 244–251. <https://doi.org/10.1148/radiol.2016151582>
- Huang, S. Y., Witzel, T., Keil, B., Scholz, A., Davids, M., Dietz, P., Rummert, E., Ramb, R., Kirsch, J. E., Yendiki, A., Fan, Q., Tian, Q., Ramos-Llordén, G., Lee, H.-H., Nummenmaa, A., Bilgic, B., Setsompop, K., Wang, F., Avram, A. V., ... Rosen, B. R. (2021). Connectome 2.0: Developing the next-generation ultra-high gradient strength human MRI scanner for bridging studies of the micro-, meso- and macro-connectome. *NeuroImage*, 243, 118530. <https://doi.org/10.1016/j.neuroimage.2021.118530>
- Javed, N., & Cascella, M. (2022). Neuroanatomy, Globus Pallidus. In *StatPearls*. Treasure Island (FL).
- Jelescu, I. O., Palombo, M., Bagnato, F., & Schilling, K. G. (2020). Challenges for biophysical modeling of microstructure. *Journal of Neuroscience Methods*, 344, 108861. <https://doi.org/10.1016/j.jneumeth.2020.108861>
- Jeurissen, B., Leemans, A., Jones, D. K., Tournier, J.-D., & Sijbers, J. (2011). Probabilistic fiber tracking using the residual bootstrap with constrained spherical deconvolution. *Human Brain Mapping*, 32(3), 461–479. <https://doi.org/10.1002/hbm.21032>
- Jones, D. K., Alexander, D. C., Bowtell, R., Cercignani, M., Dell'Acqua, F., McHugh, D. J., Miller, K. L., Palombo, M., Parker, G. J. M., Rudrapatna, U. S., Tax, C. M. W., & Tax, C. M. W. (2018). Microstructural imaging of the human brain with a “super-scanner”: 10 key advantages of ultra-strong gradients for diffusion MRI. *NeuroImage*, 182, 8–38. <https://doi.org/10.1016/j.neuroimage.2018.05.047>
- Jovicich, J., Czanner, S., Greve, D., Haley, E., van der Kouwe, A., Gollub, R., Kennedy, D., Schmitt, F., Brown, G., Macfall, J., Fischl, B., & Dale, A. (2006). Reliability in multi-site structural MRI studies: Effects of gradient non-linearity correction on phantom and human data. *NeuroImage*, 30(2), 436–443. <https://doi.org/10.1016/j.neuroimage.2005.09.046>
- Kaden, E., Kelm, N. D., Carson, R. P., Does, M. D., & Alexander, D. C. (2016a). Multi-compartment microscopic diffusion imaging. *NeuroImage*, 139, 346–359. <https://doi.org/10.1016/j.neuroimage.2016.06.002>
- Kaden, E., Kruggel, F., & Alexander, D. C. (2016b). Quantitative mapping of the per-axon diffusion coefficients in brain white matter. *Magnetic Resonance in Medicine*, 75(4), 1752–1763. <https://doi.org/10.1002/mrm.25734>
- Keil, B., Blau, J. N., Biber, S., Hoecht, P., Tountcheva, V., Setsompop, K., Triantafyllou, C., & Wald, L. L. (2013). A 64-channel 3T array coil for accelerated brain MRI. *Magnetic Resonance in Medicine*, 70(1), 248–258. <https://doi.org/10.1002/mrm.24427>
- Kiselev, V. G. (2021). Microstructure with diffusion MRI: What scale we are sensitive to? *Journal of Neuroscience Methods*, 347, 108910. <https://doi.org/10.1016/j.jneumeth.2020.108910>
- Latysheva, A., Geier, O. M., Hope, T. R., Brunetti, M., Micci, F., Vik-Mo, E. O., Emblem, K. E., & Server, A. (2020). Diagnostic utility of restriction spectrum imaging in the characterization of the peritumoral brain zone in glioblastoma: Analysis of overall and progression-free survival. *European Journal of Radiology*, 132, 109289. <https://doi.org/10.1016/j.ejrad.2020.109289>
- le Bihan, D. (1995). Molecular diffusion, tissue microdynamics and microstructure. *NMR in Biomedicine*, 8(7–8), 375–386.
- Lee, H. H., Fieremans, E., & Novikov, D. S. (2018). What dominates the time dependence of diffusion transverse to axons: Intra- or extra-axonal water? *NeuroImage*, 182, 500–510. <https://doi.org/10.1016/j.neuroimage.2017.12.038>
- McDonald, C. R., Delfanti, R. L., Krishnan, A. P., Leyden, K. M., Hattangadi-Gluth, J. A., Seibert, T. M., Karunamuni, R., Elbe, P., Kuperman, J. M., Bartsch, H., Piccioni, D. E., White, N. S., Dale, A. M., & Farid, N. (2016). Restriction spectrum imaging predicts response to bevacizumab in

- patients with high-grade glioma. *Neuro-Oncology*, 18(11), 1579–1590. <https://doi.org/10.1093/neuonc/now063>
- McNab, J. A., Edlow, B. L., Witzel, T., Huang, S. Y., Bhat, H., Heberlein, K., Feiweier, T., Liu, K., Keil, B., Cohen-Adad, J., Tisdall, M. D., Folkert, R. D., Kinney, H. C., & Wald, L. L. (2013). The human connectome project and beyond: Initial applications of 300 mT/m gradients. *NeuroImage*, 80, 234–245. <https://doi.org/10.1016/j.neuroimage.2013.05.074>
- Meynert, T., & Sachs, B. (1885). *Psychiatry: A clinical treatise on diseases of the fore-brain based upon a study of its structure, functions, and nutrition. Pt. I, the anatomy, physiology, and chemistry of the brain*. G.P. Putnam's sons.
- Morez, J., Sijbers, J., Vanhevel, F., & Jeurissen, B. (2021). Constrained spherical deconvolution of nonspherically sampled diffusion MRI data. *Human Brain Mapping*, 42(2), 521–538. <https://doi.org/10.1002/hbm.25241>
- Nilsson, M., Englund, E., Szczepankiewicz, F., van Westen, D., & Sundgren, P. C. (2018). Imaging brain tumour microstructure. *NeuroImage*, 182, 232–250. <https://doi.org/10.1016/j.neuroimage.2018.04.075>
- Nilsson, M., Lasic, S., Drobnjak, I., Topgaard, D., & Westin, C. F. (2017). Resolution limit of cylinder diameter estimation by diffusion MRI: The impact of gradient waveform and orientation dispersion. *NMR in Biomedicine*, 30(7), e3711. <https://doi.org/10.1002/nbm.3711>
- Novikov, D. S. (2021). The present and the future of microstructure MRI: From a paradigm shift to normal science. *Journal of Neuroscience Methods*, 351, 108947. <https://doi.org/10.1016/j.jneumeth.2020.108947>
- Novikov, D. S., Fieremans, E., Jespersen, S. N., & Kiselev, V. G. (2019). Quantifying brain microstructure with diffusion MRI: Theory and parameter estimation. *NMR in Biomedicine*, 32(4), e3998. <https://doi.org/10.1002/nbm.3998>
- Novikov, D. S., Kiselev, V. G., & Jespersen, S. N. (2018a). On modeling. *Magnetic Resonance in Medicine*, 79(6), 3172–3193. <https://doi.org/10.1002/mrm.27101>
- Novikov, D. S., Veraart, J., Jelescu, I. O., & Fieremans, E. (2018b). Rotationally-invariant mapping of scalar and orientational metrics of neuronal microstructure with diffusion MRI. *NeuroImage*, 174, 518–538. <https://doi.org/10.1016/j.neuroimage.2018.03.006>
- Ong, H. H., & Wehrli, F. W. (2010). Quantifying axon diameter and intracellular volume fraction in excised mouse spinal cord with q-space imaging. *NeuroImage*, 51(4), 1360–1366. <https://doi.org/10.1016/j.neuroimage.2010.03.063>
- Palombo, M., Ianus, A., Guerreri, M., Nunes, D., Alexander, D. C., Shemesh, N., & Zhang, H. (2020). SANDI: A compartment-based model for non-invasive apparent soma and neurite imaging by diffusion MRI. *NeuroImage*, 215, 116835. <https://doi.org/10.1016/j.neuroimage.2020.116835>
- Panagiotaki, E., Schneider, T., Siow, B., Hall, M. G., Lythgoe, M. F., & Alexander, D. C. (2012). Compartment models of the diffusion MR signal in brain white matter: A taxonomy and comparison. *NeuroImage*, 59(3), 2241–2254. <https://doi.org/10.1016/j.neuroimage.2011.09.081>
- Polimeni, J. R., Bhat, H., Witzel, T., Benner, T., Feiweier, T., Inati, S. J., Renvall, V., Heberlein, K., & Wald, L. L. (2016). Reducing sensitivity losses due to respiration and motion in accelerated echo planar imaging by reordering the autocalibration data acquisition. *Magnetic Resonance in Medicine*, 75(2), 665–679. <https://doi.org/10.1002/mrm.25628>
- Postelnicu, G., Zollei, L., & Fischl, B. (2009). Combined volumetric and surface registration. *IEEE Transactions on Medical Imaging*, 28(4), 508–522. <https://doi.org/10.1109/TMI.2008.2004426>
- Setsompop, K., Cohen-Adad, J., Gagoski, B. A., Raji, T., Yendiki, A., Keil, B., Wedeen, V. J., & Wald, L. L. (2012a). Improving diffusion MRI using simultaneous multi-slice echo planar imaging. *NeuroImage*, 63(1), 569–580. <https://doi.org/10.1016/j.neuroimage.2012.06.033>
- Setsompop, K., Gagoski, B. A., Polimeni, J. R., Witzel, T., Wedeen, V. J., & Wald, L. L. (2012b). Blipped-controlled aliasing in parallel imaging for simultaneous multislice echo planar imaging with reduced g-factor penalty. *Magnetic Resonance in Medicine*, 67(5), 1210–1224. <https://doi.org/10.1002/mrm.23097>
- Setsompop, K., Kimmlingen, R., Eberlein, E., Witzel, T., Cohen-Adad, J., McNab, J. A., Keil, B., Tisdall, M. D., Hoecht, P., Dietz, P., Cauley, S. F., Tountcheva, V., Matschl, V., Lenz, V. H., Heberlein, K., Potthast, A., Thein, H., van Horn, J., Toga, A., ... Wald, L. L. (2013). Pushing the limits of in vivo diffusion MRI for the human connectome project. *NeuroImage*, 80, 220–233. <https://doi.org/10.1016/j.neuroimage.2013.05.078>
- Smith, S. M., Jenkinson, M., Woolrich, M. W., Beckmann, C. F., Behrens, T. E., Johansen-Berg, H., Bannister, P. R., de Luca, M., Drobnjak, I., Flitney, D. E., Niazy, R. K., Saunders, J., Vickers, J., Zhang, Y., de Stefano, N., Brady, J. M., & Matthews, P. M. (2004). Advances in functional and structural MR image analysis and implementation as FSL. *NeuroImage*, 23(Suppl 1), S208–S219. <https://doi.org/10.1016/j.neuroimage.2004.07.051>
- Solenov, E., Watanabe, H., Manley, G. T., & Verkman, A. S. (2004). Sevenfold-reduced osmotic water permeability in primary astrocyte cultures from AQP-4-deficient mice, measured by a fluorescence quenching method. *American Journal of Physiology. Cell Physiology*, 286(2), C426–C432. <https://doi.org/10.1152/ajpcell.00298.2003>
- Stanisz, G. J., Szafer, A., Wright, G. A., & Henkelman, R. M. (1997). An analytical model of restricted diffusion in bovine optic nerve. *Magnetic Resonance in Medicine*, 37(1), 103–111. <https://doi.org/10.1002/mrm.1910370115>
- Szczepankiewicz, F., Westin, C. F., & Nilsson, M. (2021). Gradient waveform design for tensor-valued encoding in diffusion MRI. *Journal of Neuroscience Methods*, 348, 109007. <https://doi.org/10.1016/j.jneumeth.2020.109007>
- Tian, Q., Fan, Q., Witzel, T., Polackal, M. N., Ohringer, N. A., Ngamsombat, C., Russo, A. W., Machado, N., Brewer, K., Wang, F., Setsompop, K., Polimeni, J. R., Keil, B., Wald, L. L., Rosen, B. R., Klawiter, E. C., Nummenmaa, A., Huang, S. Y., & Huang, S. Y. (2022). Comprehensive diffusion MRI dataset for in vivo human brain microstructure mapping using 300 mT/m gradients. *Sci Data*, 9(1), 7. <https://doi.org/10.1038/s41597-021-01092-6>
- Tournier, J. D., Calamante, F., Gadian, D. G., & Connelly, A. (2004). Direct estimation of the fiber orientation density function from diffusion-weighted MRI data using spherical deconvolution. *NeuroImage*, 23(3), 1176–1185. <https://doi.org/10.1016/j.neuroimage.2004.07.037>
- Vachha, B., & Huang, S. Y. (2021). MRI with ultrahigh field strength and high-performance gradients: Challenges and opportunities for clinical neuroimaging at 7 T and beyond. *Eur Radiol Exp*, 5(1), 35. <https://doi.org/10.1186/s41747-021-00216-2>
- van Essen, D. C., Ugurbil, K., Auerbach, E., Barch, D., Behrens, T. E., Bucholz, R., Chang, A., Chen, L., Corbetta, M., Curtiss, S. W., Penna, S. D., Feinberg, D., Glasser, M. F., Harel, N., Heath, A. C., Larson-Prior, L., Marcus, D., Michalareas, G., Moeller, S., ... Consortium, W. U.-M. H. (2012). The human connectome project: A data acquisition perspective. *NeuroImage*, 62(4), 2222–2231. <https://doi.org/10.1016/j.neuroimage.2012.02.018>
- Veraart, J., Fieremans, E., & Novikov, D. S. (2019). On the scaling behavior of water diffusion in human brain white matter. *NeuroImage*, 185, 379–387. <https://doi.org/10.1016/j.neuroimage.2018.09.075>
- Veraart, J., Nunes, D., Rudrapatna, U., Fieremans, E., Jones, D. K., Novikov, D. S., & Shemesh, N. (2020). Noninvasive quantification of axon radii using diffusion MRI. *eLife*, 9, e49855. <https://doi.org/10.7554/eLife.49855>
- White, N. S., Leergaard, T. B., D'Arceuil, H., Bjaalie, J. G., & Dale, A. M. (2013a). Probing tissue microstructure with restriction spectrum imaging: Histological and theoretical validation. *Human Brain Mapping*, 34(2), 327–346. <https://doi.org/10.1002/hbm.21454>



- White, N. S., McDonald, C., Farid, N., Kuperman, J., Karow, D., Schenker-Ahmed, N. M., Bartsch, H., Rakow-Penner, R., Holland, D., Shabaik, A., Bjørnerud, A., Hope, T., Hattangadi-Gluth, J., Liss, M., Parsons, J. K., Chen, C. C., Raman, S., Margolis, D., Reiter, R. E., ... Dale, A. M. (2014). Diffusion-weighted imaging in cancer: Physical foundations and applications of restriction spectrum imaging. *Cancer Research*, 74(17), 4638–4652. <https://doi.org/10.1158/0008-5472.CAN-13-3534>
- White, N. S., McDonald, C. R., Farid, N., Kuperman, J. M., Kesari, S., & Dale, A. M. (2013b). Improved conspicuity and delineation of high-grade primary and metastatic brain tumors using "restriction spectrum imaging": Quantitative comparison with high B-value DWI and ADC. *AJNR. American Journal of Neuroradiology*, 34(5), 958–964, S951. <https://doi.org/10.3174/ajnr.A3327>
- Wiegell, M. R., Tuch, D. S., Larsson, H. B., & Wedeen, V. J. (2003). Automatic segmentation of thalamic nuclei from diffusion tensor magnetic resonance imaging. *NeuroImage*, 19, 391–401. [https://doi.org/10.1016/s1053-8119\(03\)00044-2](https://doi.org/10.1016/s1053-8119(03)00044-2)
- Xu, J. (2021). Probing neural tissues at small scales: Recent progress of oscillating gradient spin echo (OGSE) neuroimaging in humans. *Journal of Neuroscience Methods*, 349, 109024. <https://doi.org/10.1016/j.jneumeth.2020.109024>
- Zhang, H., Schneider, T., Wheeler-Kingshott, C. A., & Alexander, D. C. (2012). NODDI: Practical in vivo neurite orientation dispersion and density imaging of the human brain. *NeuroImage*, 61(4), 1000–1016. <https://doi.org/10.1016/j.neuroimage.2012.03.072>
- Zollei, L., Stevens, A., Huber, K., Kakunoori, S., & Fischl, B. (2010). Improved tractography alignment using combined volumetric and surface registration. *NeuroImage*, 51(1), 206–213. <https://doi.org/10.1016/j.neuroimage.2010.01.101>

#### SUPPORTING INFORMATION

Additional supporting information can be found online in the Supporting Information section at the end of this article.

**How to cite this article:** Wichtmann, B. D., Fan, Q., Eskandarian, L., Witzel, T., Attenberger, U. I., Pieper, C. C., Schad, L., Rosen, B. R., Wald, L. L., Huang, S. Y., & Nummenmaa, A. (2023). Linear multi-scale modeling of diffusion MRI data: A framework for characterization of oriented structures across length scales. *Human Brain Mapping*, 44(4), 1496–1514. <https://doi.org/10.1002/hbm.26143>